ACS APPLIED MATERIALS & INTERFACES

www.acsami.org

Research Article

High Salt-Content Plasticized Flame-Retardant Polymer Electrolytes

Lu Bai, Sina Ghiassinejad, Jérémy Brassinne, Yang Fu, Jiande Wang, Hui Yang, Alexandru Vlad, Andrea Minoia, Roberto Lazzaroni, and Jean-François Gohy*

Cite This: *ACS Appl. Mater. Interfaces* 2021, 13, 44844–44859

Read Online

ACCESS | Metrics & More | Article Recommendations | Supporting Information

ABSTRACT: New solid polymer electrolytes are of particular interest for next-generation high-energy batteries since they can overcome the limited voltage window of conventional polyether-based electrolytes. Herein, a flame-retardant phosphorus-containing polymer, poly(dimethyl(methacryloyloxy)methyl phosphonate) (PMAPC1) is introduced as a promising polymer matrix. Free-standing membranes are easily obtained by mixing PMAPC1 with lithium bis(trifluoromethanesulfonyl)imide (LiTFSI) and a small amount of acetonitrile (AN). LiTFSI/AN mixed aggregates are formed that act as plasticizers and enable ionic conductivities up to 1.6×10^{-3} S cm^{-1} at 100 °C. The high content of LiTFSI used in our electrolytes leads to the formation of a stable LiF solid-electrolyte interphase, which can effectively suppress Li dendrites and the chemical degradation of AN in contact with Li. Accordingly the electrolyte membranes exhibit a wide electrochemical stability window above 4.7 V versus Li^+/Li and fire-retardant properties due to the presence of the phosphorus-containing polymer. Atomistic molecular modeling simulations have been performed to determine the structure of the electrolytes on the microscopic scale and to rationalize the trends in ionic conductivity and the transport regime as a function of the electrolyte composition. Finally, our electrolyte membranes enable stable cycling performance for $LiFePO_4$|PMAPC1 + LiTFSI + AN|Li batteries.

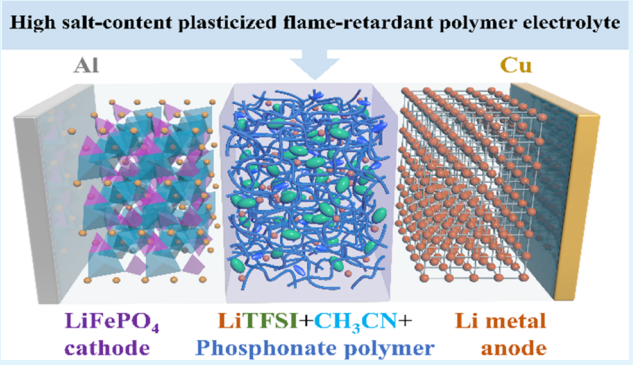

KEYWORDS: *polyethers, PMAPC1, solid polymer electrolytes, lithium-ion batteries, LiTFSI*

1. INTRODUCTION

Among the current chemical battery systems, such as consumer electronics, electric vehicles, and energy storage systems,[1] lithium-ion batteries are considered as the most promising energy storage devices due to their high energy density, long cycle life, and no memory effect.[2] In most commercial batteries, organic liquid electrolytes are used due to their high ionic conductivity and good interfacial contact. Nevertheless, their obvious drawbacks, such as volatility, flammability, decomposition, and poor safety, hinder the further development of high-energy-density lithium-ion batteries.[3] Therefore, replacing liquid electrolytes with solid-state electrolytes has been considered as the key to safe and durable lithium-based battery systems and is urgently required for the further development of lithium-metal batteries (LMBs) that rely on lithium metal as the anode.[4] Many types of polymer-based electrolytes have been proposed so far, including solid polymer electrolytes (SPEs) and gel polymer electrolytes, each of these with advantages and drawbacks under current intense studies in search for the ideal formulation.[5,6] SPEs have the advantages of safety, flexibility, light weight, and easy processing into films. They can also suppress the problems of lithium dendrites and electrolyte decomposition and are thus good candidates for LMBs.[2,7,8]

Over the past decades, many researchers have been committed to the research on SPEs based on poly(ethylene oxide) (PEO)-based polymers, trying to improve the conductivity by introducing new lithium salts, decreasing the crystallinity of PEO, and adding plasticizers or nanoparticles.[9,10] Despite these efforts, the ionic conductivity of the PEO-based SPEs remain relatively low and their limited electrochemical stability makes them only compatible with cathodes below 4 V, calling for the investigation of other types of polymers including poly(ethylene carbonate),[11] perfluoropolyether,[12] polyimine,[13] and poly(vinylene carbonate),[14] to name a few. Nevertheless, the ionic conductivity values of the SPEs based on those polymers are still low and further research is still required to approach the performances of liquid or gel electrolytes. Moreover, although their flammability is considerably reduced compared to liquid or gel electrolytes, SPEs are still flammable and cannot totally suppress dendrite growth.

Received: June 14, 2021
Published: September 10, 2021

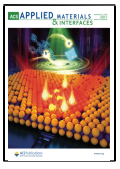

https://doi.org/10.1021/acsami.1c11058
ACS Appl. Mater. Interfaces 2021, 13, 44844–44859

Among numerous potential flame-retardant polymer electrolytes, phosphonate-containing polymers have been considered in this contribution as the most promising candidates due to their good thermal stability, bonding ability to metals, and excellent flame retardancy.[15,16] Indeed, the phosphorus atoms in phosphonates act as trapping agents for the hydrogen radicals that initiate chain reactions to cause combustion.[17] Therefore, low molar mass phosphonate-containing compounds have been widely used as fire-retardant additives in electrolyte formulations.[18,19]

Here, we propose the use of a phosphonate-containing polymer, namely, poly(dimethyl(methacryloyloxy)methyl phosphonate) (PMAPC1), that plays at the same time the role of a polymer matrix and fire-retardant agent in the formulation of our electrolytes. The lithium salt, bis-(trifluoromethanesulfonyl)imide (LiTFSI) has been selected owing to its high dissociation ability and good thermal and chemical stability.[20,21] Moreover, when LiTFSI is employed at high concentrations in the electrolyte, it can improve the interfacial compatibility and enhance the stability by forming a fluorinated solid-electrolyte interphase (SEI) film on the lithium anode surface in LMBs.[22−24] To increase the ionic mobility in our system, we have further added small amounts of acetonitrile (AN) as a plasticizer in our formulation. Indeed, AN strongly solvates lithium salts and enhances the ionic conductivity of the electrolyte due to its high dielectric constant.[25,26] Besides this, it also has a high oxidation-tolerant property and can overcome the conventional voltage limitation.[27] However, AN can spontaneously react with metal lithium violently.[28,29] Nevertheless, Yamada and coworkers have recently demonstrated that AN shows unusual electrochemical stability when small amounts of AN are mixed with LiTFSI in the superconcentrated electrolytes.[30]

In this contribution, we demonstrate that plasticized or quasi-solid polymer electrolytes containing the phosphonate-containing polymer PMAPC1, LiTFSI, and small amounts of AN allow the formation of flame-retardant self-standing flexible electrolyte membranes exhibiting high electrochemical and thermal stabilities and good ionic conductivities at 60 °C. To further characterize the microstructure of the plasticized SPEs and to get a better insight on the interactions between the PMAPC1 polymer chains, LiTFSI, and AN, a detailed molecular modeling study was performed based on molecular dynamics, MD calculations. From the MD simulations we have also determined the trend in ionic conductivity and transport regime as a function of the SPE composition. The potential application of plasticized SPEs in LMBs is demonstrated by measuring a $LiFePO_4$|SPE|Li battery that shows excellent cycling stability and good capacity retention of 100 mAh g^{-1} at 1 C when operated at 60 °C.

2. EXPERIMENTAL SECTION

2.1. Materials. The chemicals used for synthesizing the polymers were reagent grade and the chemicals used for preparing the batteries were battery grade, all used without further purification. Dimethyl hydrogenophosphonate, methacrylic acid (MAA), cyanoisopropyl dithiobenzoate (CIDB), and poly(vinylidene fluoride) (PVDF) were purchased from Sigma-Aldrich. Paraformaldehyde, dicyclohexylcarbodiimide (DCCI), *N*-methyl-2-pyrrolidone (NMP), and lithium-metal foil (99.9%) were purchased from Alfa Aesar. *N*,*N*-Dimethyl-4-aminopyridine (DMAP) was purchased from Acros. Methanol, chloroform, dimethylformamide (DMF), and diethyl ether were purchased from VWR. Potassium carbonate (K_2CO_3) was anhydrous and purchased from Fluka. 2,2′-Azobisisobutyronitrile (AIBN) was purchased from Sigma-Aldrich and recrystallized in methanol before using it. Deuterated chloroform ($CDCl_3$) used for NMR spectroscopy was purchased from Eurisotop. Lithium battery-grade lithium bis(trifluoromethanesulfonyl)imide (LiTFSI), lithium iron phosphate ($LiFePO_4$), and Super-P were purchased from Sigma-Aldrich. Acetonitrile (AN) was anhydrous and purchased from Sigma-Aldrich.

2.2. Synthesis of Dimethyl-α-hydroxymethyl Phosphonate. Dimethyl hydrogenophosphonate (20 g, 0.09 mol) and paraformaldehyde (5.46 g, 0.09 mol) were added to methanol (60 mL) in a two-neck round bottom flask equipped with a condenser. Then, anhydrous potassium carbonate (1.24 g) was introduced and stirred under reflux for 2 h. Dimethyl-α-hydroxymethyl phosphonate was obtained after removing all of the solvent under vacuum at 40 °C. ^{1}H NMR spectroscopy was used to characterize the product.

^{1}H NMR (300 MHz, $CDCl_3$, δ ppm): 3.6 (d, 6H, $PO(OCH_3)_2$); 3.9 (d, 2H, CH_2P); 5.3 (s, 1H, OH).

2.3. Synthesis of Dimethyl(methacryloxy)methyl Phosphonate (MAPC1). Dimethyl-α-hydroxymethylphosphonate (10 g, 71 mmol) and MAA (6.15 g, 71 mmol) were added to chloroform (50 mL) in a two-neck round bottom flask at 0 °C. DCCI (14.73 g, 71 mmol) and DMAP (0.872 g, 7.1 mmol) were added to the mixture under a nitrogen atmosphere. The solution was vigorously stirred for 2 h at room temperature. The final product was obtained after filtration and concentrated under vacuum. ^{1}H NMR spectroscopy was used to characterize the product.

^{1}H NMR (300 MHz, $CDCl_3$, δ ppm): 1.8 (s, 3H, $C(CH_3)-C$); 3.6 (d, 6H, $PO(OCH_3)_2$); 4.45 (d, 2H, CH_2P); 5.5 (s, H, $H_2C=C(CH_3)$); 6.1 (s, H, $H_2C=C(CH_3)$).

2.4. Reversible Addition−Fragmentation Transfer (RAFT) Polymerization of MAPC1. CIDB (44.2 mg, 0.2 mmol), AIBN (10.9 mg, 0.07 mmol), and MAPC1 (2 g, 9.6 mmol) were added to dimethylformamide (7 mL) in a Schlenk tube under a nitrogen atmosphere. The mixture was degassed by several freeze−pump−thaw cycles, and then immersed in a preheated oil bath at 70 °C for 400 min. The polymerization was stopped by exposure to the air and cooling with liquid nitrogen. Poly(dimethyl(methacryloyloxy)methyl phosphonate) (PMAPC1) was precipitated in cold hexane after DMF removal under vacuum. ^{1}H NMR spectroscopy was used to characterize the product and to determine the molar mass by comparing the intensity of the characteristic signals from the monomer to the ones of the chain transfer agent (CTA) in the aromatic region. A molar mass of 12 000 g mol^{-1} was calculated.

^{1}H NMR (300 MHz, $CDCl_3$, δ ppm): 8.0−7.2 ($H_{aromatic}$); 4.4−4.2 (CH_2-P); 4−3.7 (OCH_3), 2.2−1.9 (CH_2 backbone); 1.2−0.8 (CH_3).

In other experiments, the amounts of CIDB and AIBN were divided by 2 and 3, respectively, while the amount of MAPC1 and the polymerization time were kept constant compared to the experiment described here above. This resulted in PMAPC1 homopolymers with molar masses of 18 000 and 24 000 g mol^{-1}, respectively.

2.5. Electrolyte Preparation. The electrolytes were prepared according to the following steps. First, a specified amount of PMAPC1 was dissolved in AN with mild stirring to prepare a homogeneous mixture. Then, LiTFSI was added to the mixture in different molar ratios. After continuously stirring at room temperature for 24 h, the solutions were cast on a Teflon mold, and then dried inside the glovebox at room temperature for 12 h. Subsequently, they were dried in a dynamic vacuum oven at 100 °C overnight to remove the solvent completely. After this, the mold was transferred back to the glovebox immediately to minimize the absorption of water from the air. They were weighed to determine the amount of dried PMAPC1 and LiTFSI in the mold and to further calculate the amount of AN to be added. After addition of the required amount of AN to the dried PMAPC1 and LiTFSI in the glovebox, the SPE was obtained. To allow homogeneous dispersion of AN within the SPE, each membrane was equilibrated for 2 days before measurements. For each investigated SPE composition, three samples were prepared to assess reproducibility of the results.

2.6. Experimental Techniques. Nuclear magnetic resonance (NMR) spectroscopy was conducted using a Bruker 300 UltraShield

https://doi.org/10.1021/acsami.1c11058
ACS Appl. Mater. Interfaces 2021, 13, 44844−44859

spectrometer. The monomers and polymer were dissolved in deuterated chloroform ($CDCl_3$).

Size exclusion chromatography (SEC) was performed on an Agilent system with 1 mL min^{-1} DMF (containing 0.1 wt % of LiCl) as the eluent. Poly(methyl methacrylate) standards were used for calibration.

Fourier-transform infrared (FTIR) spectra were measured using an Agilent Technologies Cary 630 FTIR using a diamond attenuated total reflection (ATR) unit with the wavelength from 4000 to 650 cm^{-1} under an argon atmosphere.

Differential scanning calorimetry (DSC) was conducted using a Mettler Toledo DSC1 equipped with STARe software. Samples were placed in a 40 μL sealed aluminum pan. The temperature profile was swept from −70 to 130 °C at a heating rate of 10 °C min^{-1} under a nitrogen atmosphere.

Thermogravimetric analysis (TGA) was conducted using a Netzsch STA 449F3. Samples were placed in an 85 μL alumina crucible under a constant argon flow with a heating rate of 5 K min^{-1}, and initial and final temperatures were set at 25 and 500 °C, respectively.

Viscoelastic properties of all samples were investigated by small amplitude oscillatory shear rheology using an MCR 301 (Anton Paar, Germany) rheometer. Temperature was controlled using a convection oven operating under a small nitrogen flow rate for measuring in the temperature range between 20 and 120 °C. A parallel plate geometry (diameter 8 mm) was used depending on the viscosity level of the system at the given temperature. No slip problem was observed due to good adhesion of the phosphonate polymers to the surface of the steel geometry. A series of amplitude sweeps confirmed that all of the measurements were performed in the linear viscoelastic regime (1%). For the melt-state measurements, the samples were loaded at 120 °C and stabilized for 1 h. Then, the sequence frequency sweeps started by a 20 °C temperature gap until 40 °C. For checking the reproducibility of measurements, all measurements were repeated from 40 to 120 °C and the data were identical. For the solution measurements, equilibration was achieved at low temperature to avoid solvent evaporation and then a set of frequency sweeps from 20 °C until 60 °C have been measured.

Scanning electron microscopy (SEM) images were obtained with a field-emission SEM JEOL 7600F operating at 15 kV.

X-ray powder diffraction (XRD) patterns were collected on a STOE Darmstadt transmission diffractometer system using Cu Kα radiation with a wavelength of 1.54 Å.

X-ray photoelectron spectroscopy (XPS) was performed using an SSI X-Probe (SSX 100/206) photoelectron spectrometer from Surface Science Instruments equipped with a monochromatized Al Kα X-ray source. The batteries were disassembled in a glovebox after cycling, and the electrodes were washed with dimethyl carbonate (DMC) before transfering into the XPS chamber. All of the binding energies were calculated according to the C−(C, H) component of the C 1s peak fixed at 284.8 eV. Data analysis was carried out using CasaXPS software, and the peaks were decomposed using the Gaussian/Lorentzian product formula GL(15) after a Shirley-type background was subtracted.

Electrochemical impedance spectroscopy (EIS) was conducted on the electrolytes assembled into a symmetrical stainless steel (SS)|SPE|SS configuration for measuring the ionic conductivity. A Bio-Logic VMP-300 potentiostat was used for measuring EIS at a voltage amplitude of 10 mV and a frequency range of 7 MHz to 0.1 Hz. For measuring the temperature dependent ionic conductivity, the cells were placed in a temperature-controlled chamber. All of the measurements were carried out from 100 to 20 °C by a programmed instruction, with a decreasing step of 20 °C and an equilibration time of 2 h between each step.

Linear sweep voltammetry (LSV) was applied to evaluate the electrochemical window in a Li|SPE|SS configuration, with stainless steel (SS) as a working electrode and Li metal as both the reference electrode and the counter electrode. Using a Bio-Logic VMP-300 potentiostat, the LSV was measured under 60 °C in the potential range from 0 to 6 V at a scanning rate of 1 mV s^{-1}.

The interface stability between the electrolyte and the lithium-metal electrode was measured by a galvanostatic cycling experiment in symmetrical Li|SPE|Li cells. The battery was charged and discharged repeatedly for 1 h with a specific current density of 1 mA cm^{-2} at 60 °C using a NEWARE battery test system.

The electrolyte was assembled in symmetrical Li|SPE|Li cells for transference number measurements. Those measurements including DC polarization and EIS were performed with a Bio-Logic VMP-300 potentiostat at 60 °C. The impedance measurements were performed as mentioned above, and the polarization with a DC bias of 50 mV was performed until a plateau in current was reached.

2.7. Fabrication of Full Batteries. $LiFePO_4$, carbon black (Super-P), 1PMAPC1 + 2LiTFSI + 1AN, and a poly(vinylidene fluoride) (PVDF) binder were dispersed in an *N*-methyl-2-pyrrolidone (NMP) solvent with a weight ratio of 30:30:35:5. The obtained slurry was uniformly spread on a carbon-coated aluminum current collector with a knife coater, followed by drying in a dynamic vacuum oven at 100 °C for 24 h. The obtained electrode sheets were punched out to disks as the cathode in coin cells. The lithium foil was polished carefully and used as the anode. 1PMAPC1 + 2LiTFSI + 1AN was used as SPE. The electrode and electrolyte were assembled in a CR2032-type coin cell with a Li|SPE|$LiFePO_4$ configuration for charge/discharge tests on a NEWARE battery test system.

3. THEORETICAL CALCULATIONS

3.1. Electrostatic and Polarization Effects. All atomistic molecular dynamics simulations in this study have been carried out using the GROMACS 2018[31] molecular code and a modified version of the OPLS-AA force field,[32] where the atomic charges for the LiTFSI salt have been derived at the quantum chemistry level. In particular, all Li^+ cations have their nominal charge of +1, to account for the possibility of full salt dissociation, while for $TFSI^-$ we used the electrostatic potential (ESP) atomic charges obtained from quantum chemical calculations at the MP2 level of theory. To mimic polarization effects in the electrolytes, all electrostatic interactions have been scaled by a factor, ε_r, which depends on the electronic dielectric constant of the medium,[33,34] ε_{el}, according to eq 1.

$$\varepsilon_r = 1 - \frac{1}{\varepsilon_{el}} \tag{1}$$

Because of its abundance relative to the other species in the electrolytes, we consider the medium to be LiTFSI. Since the electronic dielectric constant of the medium is equal to the square of the refractive index, n, (1.38[35] for LiTFSI), we replaced ε_{el} with n^2 in eq 1, obtaining that the electrostatic interactions must be scaled by a factor $\varepsilon_r \sim 0.5$ in the molecular dynamics simulation.

3.2. Structure and Composition of the Modeled Electrolytes. Three PMAPC1/AN/LiTFSI SPEs have been modeled, with molecular ratios (based on the monomer units) equal to 1:1:1, 1:1:2, and 1:1:4. In all systems, the number of AN molecules was set to 256 and the number of LiTFSI and PMAPC1 chains was determined according to the molecular ratio considered. For the SPEs, this results in building a polymeric matrix that is formed by 8 interdigitated PMAPC1 polymer chains, each containing 32 monomer units, for a molecular weight of 8000 g mol^{-1}. After construction, all systems were equilibrated at 300 K and 1 atm through a series of MD runs in the NPT (constant number of particles, pressure, and temperature) and NVT (constant number of particles, volume, and temperature) ensembles. After equilibration, a production run of 40 ns, at 300 K was performed, from which all data were analyzed. During the MD simulations, the

https://doi.org/10.1021/acsami.1c11058
ACS Appl. Mater. Interfaces 2021, 13, 44844−44859

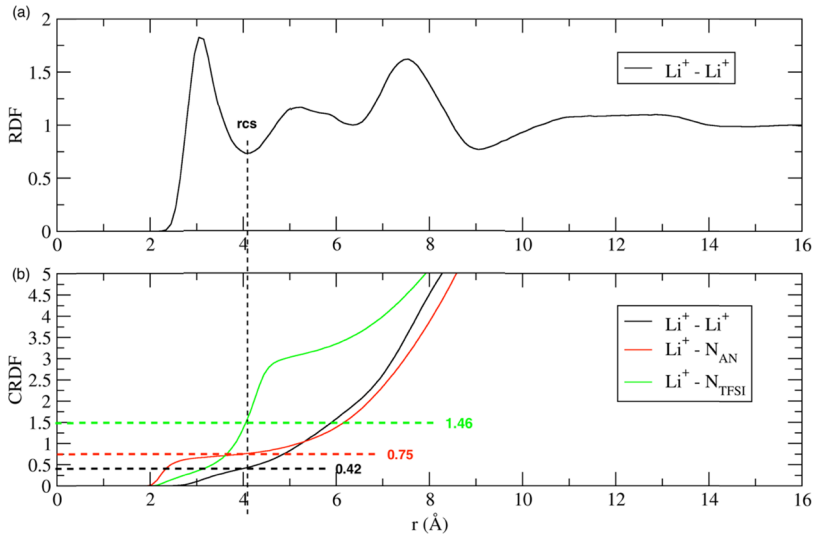

Figure 1. MD simulations of the 1PMAPC1 + 1LiTFSI + 1AN electrolyte: (a) Li^+−Li^+ RDF with the position of the Li^+ coordination shell (rcs) and (b) CDRFs for Li^+−Li^+, Li^+−N_{AN}, and Li^+−N_{TFSI}^- with an indication of the average number of interactions.

temperature and pressure were controlled with the Nose−Hoover thermostat and the Parrinello−Rahman barostat, respectively. Three-dimensional (3D) periodic boundary conditions were applied to a cubic modeling cell, to model bulk electrolytes.

3.3. Electrolyte Microstructure Characterization. The microstructure of the modeled electrolytes was investigated by means of the radial distribution functions, RDFs, between pairs of atomic and/or molecular species. From the RDF between pairs of Li^+ cations, we extract the size of the Li^+ coordination shell, which corresponds to the first minimum in the RDF after the first peak (Figure 1a). Once the size of the coordination shell for an atomic species has been defined, we consider the cumulative radial distribution functions, CRDFs, to obtain the average number of the short-range interactions between the species considered (Figure 1b).

3.4. Theoretical Ion Transport Properties and Ionic Conductivity. Two mechanisms are possible for the ions to diffuse in the electrolyte: (1) the vehicular mechanism and the (2) hopping mechanism. In the vehicular regime, the cations diffuse together with their coordination shell, while in the hopping regime the ions diffuse by exchanging ions and solvent molecules that are in their coordination shell. By calculating the degree of uncorrelated ion mobility, α, we can determine the type of ion transport mechanism that occurs in the electrolyte. This quantity is defined as the ratio of the true ionic conductivity in the system, λ, and the ideal one, for which the ions are supposed to diffuse independently from the others (λ_{uncorr}).[36]

$$\alpha = \frac{\lambda}{\lambda_{uncorr}} = \lim_{t\to\infty} \alpha(t) = \lim_{t\to\infty} \frac{\lambda^{app}(t)}{\lambda^{app}_{uncorr}(t)} \tag{2}$$

$$\lambda = \lim_{t\to\infty} \lambda^{app}(t) = \lim_{t\to\infty} \frac{e^2}{6tVk_bT} \sum_{ij}^{N} z_i z_j \langle [R_i(t) - R_i(0)][R_j(t) - R_j(0)] \rangle \tag{3}$$

The ideal ionic conductivity, λ_{uncorr} is calculated as follows

$$\lambda^{app}_{uncorr}(t) = \lim_{t\to\infty} \lambda^{app}_{uncorr}(t) = \frac{e^2}{6tVk_bT} \sum_{i}^{N} z_i^2 \langle [R_i(t) - R_i(0)]^2 \rangle \tag{4}$$

where in eqs 2 and 3, e is the electron charge, V is the volume of the simulation box, k_b is the Boltzmann constant, T is the temperature, z_i and z_j are the charges of the ions, N is the total number of ions in the simulation box, and $R_i(t)$ is the position of ion i at time t. The degree of uncorrelated ion mobility varies from 1, for the ideal case of totally independent ions, to 0, where the ions move together. It is considered that for α smaller than 0.4, the ions diffuse with a vehicular mechanism. If α is larger than 0.6, then the ions move independently from each other, using a hopping mechanism. For values of α that are between 0.4 and 0.6, the transport occurs in a mixed regime.

3.5. Validation of the Molecular Modeling Approach. The modeling strategy was validated against experimental data and results from the literature, in particular from the work of Yamada et al.[30] To test the ability of the standard OPLS-AA force field to reproduce the properties of pure AN at room temperature, we calculated the density and self-diffusion coefficient, D, for the AN molecules in a simulation box containing 512 AN molecules and compared the values against experimental data (Table S1). The comparison shows a very good quantitative agreement with the experimental density and a good qualitative one for the diffusion coefficient.

Finally, we calculate the ionic conductivity for the AN/LiTFSI 2:1 liquid electrolyte already investigated by Yamada et al. Our results show that the degree of uncorrelated ionic mobility, α, is about 0.6, meaning that the ionic transport occurs in a mixed hopping/vehicular regime, with a somewhat larger hopping character. The theoretical ionic conductivity we calculated for this electrolyte is 4.6 mS cm^{-1}, which is an overestimation by a factor of 5 with respect to the value obtained in ref 30. This is due to the fact that due to the complexity of the SPEs involved in this work, we have to rely on classical force-field MD simulations instead of the ab initio MD approach used in ref 30. Nevertheless, we can consider

https://doi.org/10.1021/acsami.1c11058
ACS Appl. Mater. Interfaces 2021, 13, 44844−44859

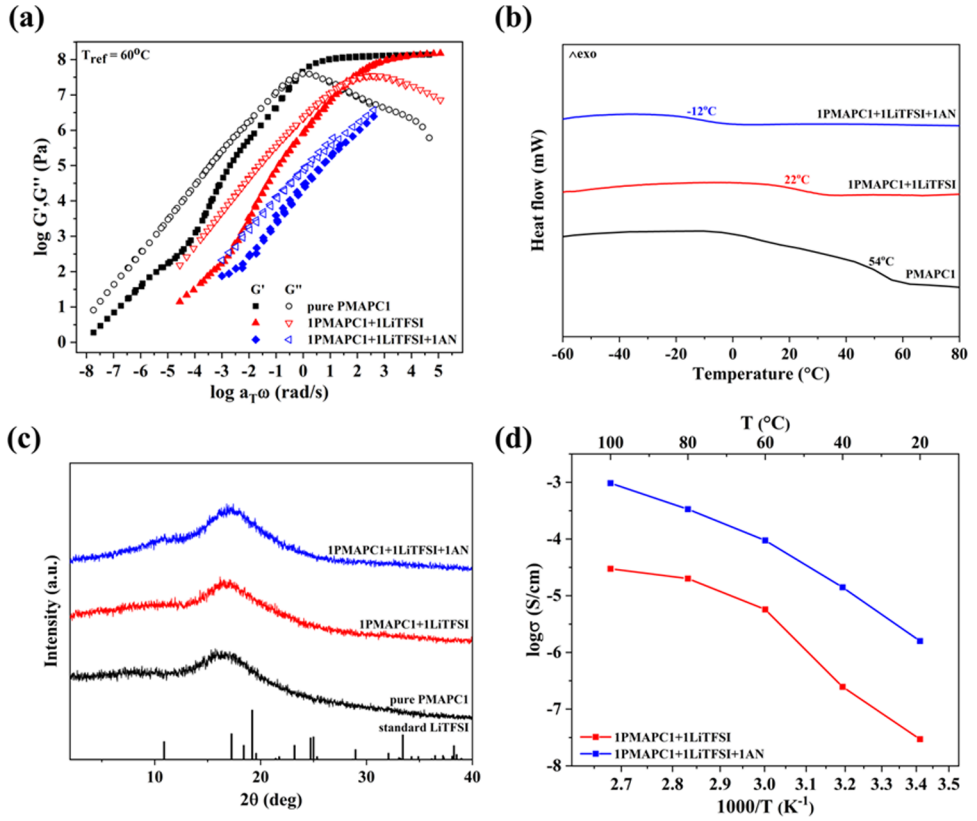

Figure 2. (a) Master curves of the storage and loss moduli, $\log(G', G'')$, as a function of angular frequency $\log \omega$ for PMAPC1, 1PMAPC1 + 1LiTFSI, and 1PMAPC1 + 1LiTFSI + 1AN. (b) DSC curves of PMAPC1, 1PMAPC1 + 1LiTFSI, and 1PMAPC1 + 1LiTFSI + 1AN. (c) XRD patterns of PMAPC1, 1PMAPC1 + 1LiTFSI, and 1PMAPC1 + 1LiTFSI + 1AN. (d) Arrhenius plots of ionic conductivity for 1PMAPC1 + 1LiTFSI and 1PMAPC1 + 1LiTFSI + 1AN.

that our results are in good qualitative agreement with those from the work of Yamada et al.

4. RESULTS AND DISCUSSION

4.1. Synthesis and Properties of PMAPC1 + LiTFSI + AN Electrolytes. The dimethyl (methacryloyloxy)methyl phosphonate monomer and its homopolymer (PMAPC1) were synthetized following a previously reported methodology.[37,38] The reversible addition−fragmentation transfer (RAFT) polymerization process was used since this technique allows the synthesis of polymers with well-defined characteristic features such as molar mass and dispersity. The synthetic route to PMAPC1 is depicted in Figure S1 while Figure S2 shows a representative ^{1}H NMR spectrum of PMAPC1, which confirms the purity of the obtained polymer with no ethylenic protons detected. SEC analysis confirmed that only one population of PMAPC1 chains with a dispersity of 1.18 was obtained. The glass transition temperature (T_g) of PMAPC1 was measured at 54 °C by differential scanning calorimetry (DSC, Figure S3a), and its thermal decomposition starts at 170 °C as measured by thermogravimetric analysis (TGA, Figure S3b). Since the molar mass of the PMAPC1 polymer is expected to influence the properties of the final electrolytes and specifically their ionic conductivity, this parameter was varied. Therefore, PMAPC1 homopolymers with different molar masses were synthesized and loaded with LiTFSI with an initial salt loading MAPC1/Li^+ (mol/mol) = 1:1. Figure S4 shows the measured ionic conductivities of the accordingly obtained SPEs at different temperatures. The best result was obtained with the PMAPC1 sample with the lowest molar mass (12 000 g mol^{-1}). This polymer was thus systematically used for the further investigations described in this contribution.

The ionic conductivity values reported in Figure S4 for PMAPC1/LiTFSI SPEs are far too low for practical utilization in batteries. Moreover, the obtained membranes are rigid and brittle, as shown in Figure S5a,b. Therefore, we set out to add acetonitrile (AN) as a plasticizer in the PMAPC1/LiTFSI SPEs to address these issues. There are three main expected effects of AN: (i) increasing the segmental motion in PMAPC1 and thus decreasing its T_g; (ii) loosening interactions between Li^+ ions and polymer chains by promoting dissociation of LiTFSI and further enhancing ion mobility by lowering the activation energy;[39] and (iii) increasing the amount of dissolved lithium salts due to the high dielectric constant of AN. To minimize safety issues such as leakage and flammability concerns caused by large amounts of organic additives[40] and the inherent reactivity of AN with metallic lithium,[28,41] only small amounts of AN have been added to the PMAPC1 SPEs. These amounts have been calculated in terms of molar ratios relative to LiTFSI and PMAPC1.

The beneficial effect of the addition of AN can be directly visualized by comparing the electrolyte membranes prepared from 1PMAPC1 + 1LiTFSI and 1PMAPC1 + 1LiTFSI + 1AN in Figure S5 (in the following, the molar ratios of the different components of the electrolytes will be indicated as numbers before each component, this means, for example, that a 1:1:1 mol/mol/mol MAPC1/LiTFSI/AN has been used for the 1PMAPC1 + 1LiTFSI + 1AN sample). Indeed, a flexible self-

https://doi.org/10.1021/acsami.1c11058
ACS Appl. Mater. Interfaces 2021, 13, 44844−44859

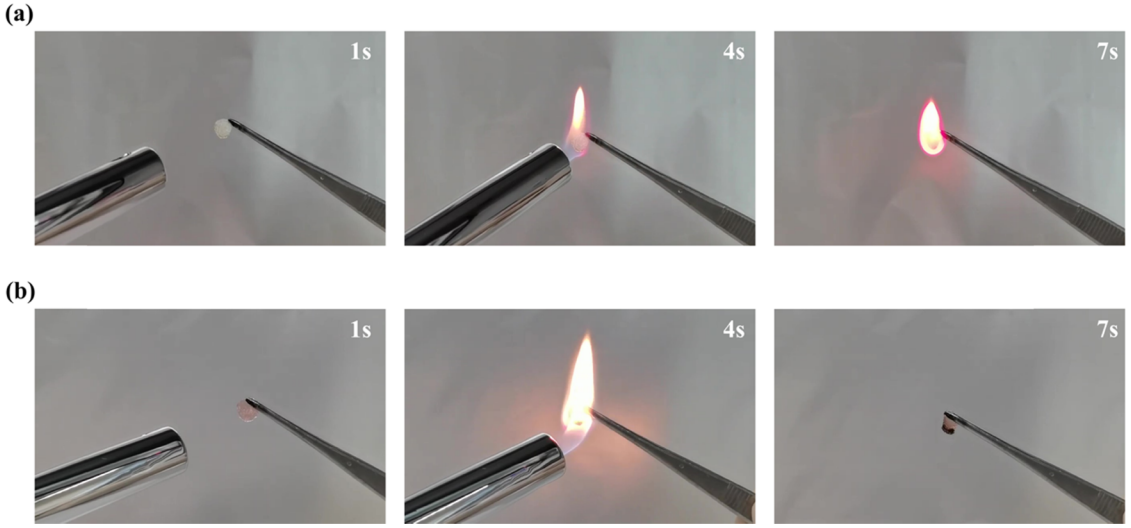

Figure 3. Flammability test of (a) 1PEO + 2LiTFSI + 1AN electrolyte and (b) 1PMAPC1 + 2LiTFSI + 1AN electrolyte.

standing membrane is observed in the case of 1PMAPC1 + 1LiTFSI + 1AN SPE, while a brittle membrane is formed for the 1PMAPC1 + 1LiTFSI membrane (Figure S5). This qualitative observation has been further confirmed by measurements of rheological properties.

Figure 2a shows the rheological data obtained for the pure PMAPC1 homopolymer as a reference, the 1PMAPC1 + 1LiTFSI SPE, and the 1PMAPC1 + 1LiTFSI + 1AN plasticized SPE. Frequency sweeps have been measured for all samples in the temperature range from 120 to 40 °C in the linear viscoelastic regime. Master curves have been constructed at a reference temperature of 60 °C based on the shift factors calculated from the William−Landel−Ferry (WLF) equation.[42] From Figure 2a, it is clearly observed that the elasticity and the relaxation time (the inverse of the angular frequency of the crossover between G' and G'') decrease when LiTFSI is added to PMAPC1. Further decreases in G', G'' and relaxation times are observed when AN is added, confirming the plasticizing effect of AN. The frequency sweeps measured at different temperatures show lower elasticity and a shorter relaxation time for the comparison of the 1PMAPC1 + 1LiTFSI and 1PMAPC1 + 1LiTFSI + 1AN samples to pure PMAPC1, and this can be attributed to the migration of ion hopping.[43] Indeed, during an ion-hopping event, the migrating ion pair is no longer anchored to the polymer chain to which it was initially attached. Therefore, the polymer chain segments in the vicinity of this ion pair experience an increase in mobility during an ion-hopping process. This mobility increment leads to a decrease in the storage modulus for the 1PMAPC1 + 1LiTFSI and 1PMAPC1 + 1LiTFSI + 1AN samples in comparison to the pure PMAPC1 homopolymer, which is more pronounced at higher temperatures (or lower angular frequencies).[44] These results are in line with the T_gs of the different samples, as shown in Figure 2b. In this respect, the T_g of PMAPC1 observed at 54 °C decreases to 22 °C for the 1PMAPC1 + 1LiTFSI sample and is further lowered to −12 °C for the 1PMAPC1 + 1LiTFSI + 1AN in agreement with the increased chain segment mobility upon addition of the LiTFSI salt and AN plasticizer. Furthermore, the observation of a single T_g for the 1PMAPC1 + 1LiTFSI and 1PMAPC1 + 1LiTFSI + 1AN samples confirms the formation of a single polymer phase with no phase-separated polymer-rich or salt-rich domains. The homogeneity of the 1PMAPC1 + 1LiTFSI and 1PMAPC1 + 1LiTFSI + 1AN samples at the nanoscale is further confirmed by X-ray diffraction (XRD) patterns (Figure 2c) in which only a broad peak associated with the PMAPC1 polymer is observed with no peaks due to LiTFSI crystalline domains.[45]

Finally, the beneficial effect of increased mobility upon addition of AN as the plasticizer is reflected in the ionic conductivities. Figure 2d reports the ionic conductivities measured by electrochemical impedance spectroscopy (EIS) on the 1PMAPC1 + 1LiTFSI and 1PMAPC1 + 1LiTFSI + 1AN samples as a function of temperature. Indeed, ionic conductivities are systematically higher for the 1PMAPC1 + 1LiTFSI + 1AN sample. Ionic conductivities in the 10^{-3} S cm^{-1} range have been measured at 100 °C with high reproducibility for the 1PMAPC1 + 1LiTFSI + 1AN sample although the boiling point of AN is 82 °C. This suggests that AN molecules are somewhat captured in the sample.

As stated in Section 1, the choice of a phosphate-containing polymer in the SPEs investigated here was motivated by the fire-retardant properties of phosphorus-containing compounds, which can be highly beneficial for LMBs. To assess the fire-retardant properties of our electrolytes, we compared them with a classical PEO-based electrolyte with a similar chemical composition.[17] Figure 3 shows the flammability test for the reference 1PEO + 2LiTFSI + 1AN electrolyte compared with the 1PMAPC1 + 2LiTFSI + 1AN electrolyte prepared in this work. As shown in Figure 3, the conventional PEO-based electrolyte caught fire immediately on ignition and the combustion continued even after the flame was removed, indicating its poor fire-resistance. In contrast, the PMAPC1-based electrolyte did not catch fire after removal from the fire torch, and thus exhibits good fire retardancy. The corresponding videos of these flammability tests are available in the Supporting Information section. The flammability tests comparing pure PEO and pure PMAPC1 polymers are shown in Figure S6a,b while the comparison between 1PEO + 2LiTFSI and 1PMAPC1 + 2LiTFSI electrolytes is depicted in Figure S6c,d. These additional flammability tests confirm the fire-retardant properties of PMAPC1-containing samples.

4.2. Optimization of the PMAPC1 + LiTFSI + AN Electrolyte Composition. On the basis of these results, we

https://doi.org/10.1021/acsami.1c11058
ACS Appl. Mater. Interfaces 2021, 13, 44844−44859

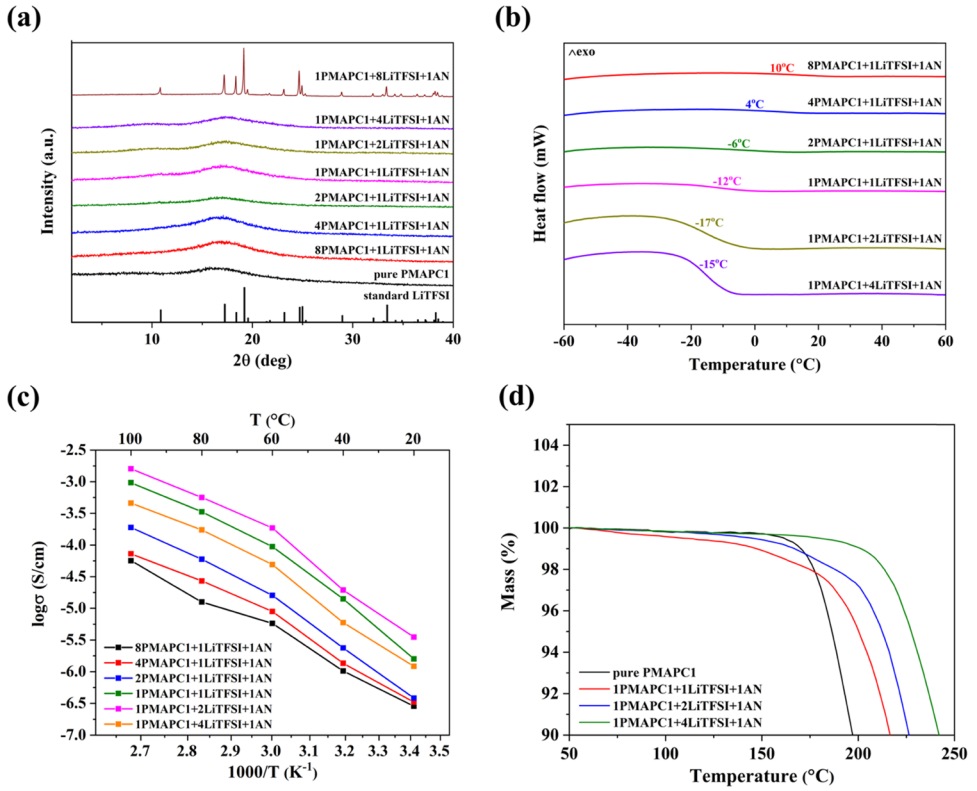

Figure 4. (a) XRD patterns of PMAPC1 and *x*PMAPC1 + *y*LiTFSI + 1AN. (b) DSC curves of *x*PMAPC1 + *y*LiTFSI + 1AN. (c) Arrhenius plots of the ionic conductivity for *x*PMAPC1 + *y*LiTFSI + 1AN. (d) TGA curves of PMAPC1 and 1PMAPC1 + *x*LiTFSI + 1AN.

decided to focus on PMAPC1 + LiTFSI + AN samples that present a higher ionic conductivity and are thus more promising for application in LMBs. This system has been further optimized by varying the MAPC1/LiTFSI ratio (from an MAPC1/LiTFSI mol/mol ratio of 8:1−1:8) and keeping the AN molar ratio to LiTFSI at 1. XRD data show homogeneous samples with no LiTFSI crystalline domains until the extreme MAPC1/Li^+ molar ratio of 1:8 (Figure 4a). The T_g of the PMAPC1 + LiTFSI + AN samples decreases with the amount of the added LiTFSI salt and reaches a minimum for an MAPC1/LiTFSI mol/mol ratio of 1:2 (Figures 4b and S7), in agreement with results previously reported by others.[46,47] At higher LiTFSI loading, the T_g starts to increase because the high salt concentration results in the increase of polymer segment−salt interactions that are not counterbalanced by ion-hopping events and the overall mobility decreases.[48−50] Moreover, the intensity of the T_g signal (estimated as the difference between the baseline level before and after T_g) in the DSC curve increases with the amount of LiTFSI and is an indication of the increase of amorphous phase dynamics.[46,47,51] The ionic conductivity measurements by EIS are shown in Figure 4c and confirm the hypothesis that the motion of ions is directly related to the T_g of the SPE since the highest ionic conductivities are measured for the lowest T_g 1PMAPC1 + 2LiTFSI + 1AN sample, whatever the temperature and reach a value of 1.6×10^{-3} S cm^{-1} at 100 °C.

To gain a deeper insight into the polymer dynamics as a function of salt loading and the comparison with the DSC and EIS measurements discussed here, rheological measurements have been performed in the temperature range from 20 to 60 °C on the 1PMAPC1 + *x*LiTFSI + 1AN electrolytes with the *x* molar ratio equal to 1, 2, and 4 (lower molar ratios of LiTFSI have not been measured since they lead to too low ionic conductivities for practical application and the sample with $x = 8$ is heterogeneous, see Figure 4a, and brittle). The frequency sweeps measured for these samples (Figure S8) show that the storage modulus of each sample decreases with increasing temperature, as a result of the higher mobility of polymer chain segments and the dynamic hopping of ions between polymer chains, as discussed earlier. Interestingly, the 1PMAPC1 + 2LiTFSI + 1AN electrolyte displays the lowest storage modulus and conversely the fastest dynamics. This is completely in agreement with the T_gs and the ionic conductivity measurements depicted in Figure 4b,c. Finally, the thermal stability of the PMAPC1 + LiTFSI + AN has been determined by thermogravimetric analysis (TGA, Figure 4d). The thermal stability of PMAPC1 + LiTFSI + AN samples is much higher than that of the PMAPC1 homopolymer. The interaction between polymer segments and the LiTFSI salt are thought to be at the origin of this thermal stabilization. Moreover, specific interactions between LiTFSI and AN also play an important role. Indeed, a slight weight loss that can be attributed to the release of AN molecules is delayed at 130 and 180 °C for the 1PMAPC1 + 2LiTFSI + 1AN and 1PMAPC1 + 4LiTFSI + 1AN samples, respectively (Figure 4d).

4.3. Understanding Ionic Conduction in PMAPC1 + LiTFSI + AN Electrolytes on the Basis of Interactions between the Components. To understand the transport properties, theoretical calculations on model systems for the SPEs have been performed. The ionic conductivity was calculated for 1PMAPC1 + 1LiTFSI + 1AN, 1PMAPC1 + 2LiTFSI + 1AN, and 1PMAPC1 + 4LiTFSI + 1AN samples and the main mechanism through which the ionic conductivity

https://doi.org/10.1021/acsami.1c11058
ACS Appl. Mater. Interfaces 2021, 13, 44844−44859

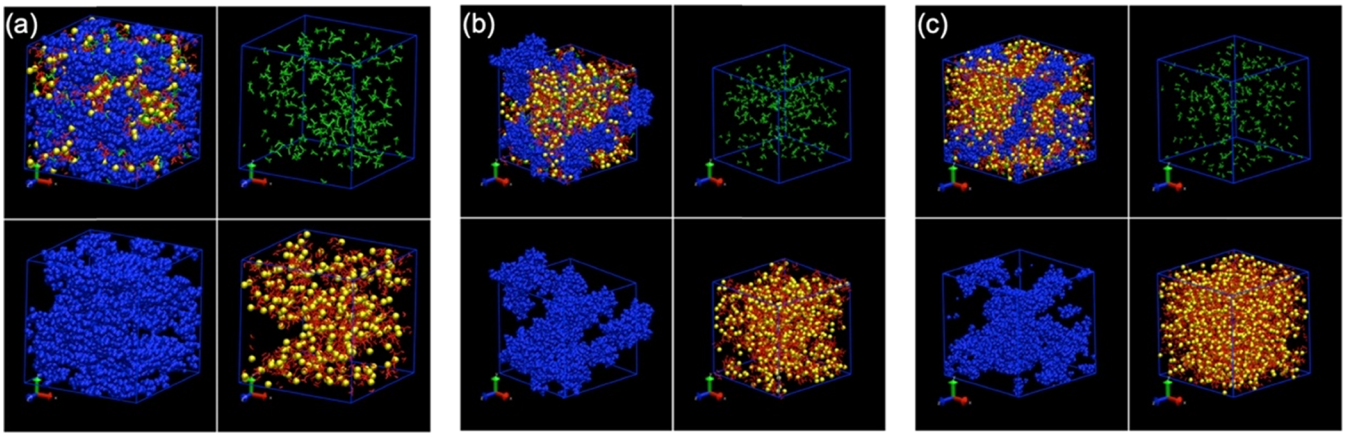

Figure 5. Structure and component distribution of (a) 1PMAPC1 + 1LiTFSI + 1AN, (b) 1PMAPC1 + 2LiTFSI + 1AN, and (c) 1PMAPC1 + 4LiTFSI + 1AN. The AN molecules are shown in green, the PMAPC1 matrix in blue, Li^+ cations in yellow, and the $TFSI^-$ anions in red.

occurs, either vehicular, or hopping, or with a mixed vehicular/hopping character, has been identified. For each SPE, the density and the diffusion coefficients were calculated for AN and both Li^+ and $TFSI^-$ ions separately. We find that AN in the SPE has a diffusion coefficient of 2−3 orders of magnitude lower than in the pure AN liquid (compare the data in Tables S1 and S2), which suggests that the AN molecules are entrapped in the SPEs due to the high amount of LiTFSI. Consistently, the diffusion of AN is further reduced on increasing the amount of LiTFSI in the electrolyte. Indeed, the diffusion of the ions also drops considerably in 1PMAPC1 + 4LiTFSI + 1AN.

For each SPE model, the ionic conductivity was calculated at room temperature (Table S3): the trend for the different SPEs is in good qualitative agreement with the experimental one (the discrepancies in the absolute values obtained from the calculations are a well-known issue, due to the description of the polarization effects by the force field).[52] The modeling indeed shows that 1PMAPC1 + 1LiTFSI + 1AN and 1PMAPC1 + 2LiTFSI + 1AN are the SPEs with higher conductivity, with the latter being the most conductive. The degree of uncorrelated ion mobility, α, allows getting a better insight into the mechanism responsible for the ionic conductivity (Table S4). While in 1PMAPC1 + 1LiTFSI + 1AN SPE the ionic transport clearly occurs with a hopping mechanism, in the other two electrolytes the ionic transport occurs in a mixed vehicular/hopping regime, although with the hopping character still dominant.

To further confirm the hypothesis that AN molecules are entrapped in the electrolytes, we have investigated the composition of the coordination shell for the nitrogen atom of the acetonitrile, N_{AN}, in the models for the three SPEs. In particular, we determined how many N_{AN}, Li^+ cations, and $TFSI^-$ anions an N_{AN} atom interacts with in its coordination shell. The results are summarized in Table S5. By increasing the amount of LiTFSI in the SPEs, each N_{AN} atom interacts, on average, with more Li^+ and $TFSI^-$, while the number of interactions with other N_{AN} decreases. In all electrolytes, the number of N_{AN}−N_{AN} contacts is much smaller than in the pure solvent, which indicates that the AN molecules are homogeneously dispersed in the LiTFSI environment rather than forming a separate AN phase, as shown by the snapshots in Figure 5 extracted at the end of the MD simulations. Altogether, these theoretical data suggest that AN is able to form a stable coordinated species with LiTFSI.

To get more information about interactions among PMAPC1, LiTFSI, and AN, Fourier-transform infrared (FTIR) spectra were recorded on PMAPC1 + LiTFSI + AN with various LiTFSI loadings (Figure 6a). In a first step, we focused on the aliphatic nitrile C≡N stretching band that is expected to appear at 2258 cm^{-1} in free AN molecules and to shift to 2278−2282 cm^{-1} when Li^+ ions are coordinated to AN molecules.[53,54] Figure 6b shows no peak for free AN molecules but only a peak at ca. 2280 cm^{-1} corresponding to AN coordinated to Li^+ ions. Furthermore, this characteristic peak shifts to higher wavenumbers with increasing salt concentrations, suggesting a more stable coordination structure as more Li^+ ions are present. This confirms the theoretical findings of favorable interactions between AN and LiTFSI, as the N_{AN} atoms interact with an ever-increasing number of Li^+ cations when increasing the amount of LiTFSI present in the electrolyte (Table S4). Figure 6c sheds light on the area between 730 and 750 cm^{-1}, which is characteristic of S−N, N−S−O, F−C−S, and C−F bonds in $TFSI^-$ anions.[30,53,54] According to the literature, the position of these peaks can be directly related to the structure of the LiTFSI ion pairs.[30,53,54] In this respect, the peak at 739 cm^{-1} arises from free $TFSI^-$ anions (solvent-separated ion pairs), the peak at 744 cm^{-1} is characteristic of contact ion pairs (CIPs, one $TFSI^-$ anion associated with one single Li^+ cation), and the peak at 748 cm^{-1} is the signature of aggregates (AGGs, one $TFSI^-$ anion coordinating to two or more Li^+ cations), respectively.[30,53,54] From the spectra shown in Figure 5c, we can deduce that free $TFSI^-$ anions disappear at the expense of CIPs and AGGs upon increasing the amount of LiTFSI in the PMAPC1 + LiTFSI + AN electrolytes. The composition of the coordination shell for the Li^+ cations obtained from the models (Table S5) also shows that by increasing the amount of LiTFSI present in the electrolyte, each Li^+ interacts with more than one nitrogen of the $TFSI^-$ anions, i.e., with more than one anion, thus confirming the absence of free $TFSI^-$ anions in the system and the tendency of the salt to form small clusters. On average, each Li^+ cation sees in its coordination shell a number of N_{AN} atoms comprised between 0.75 and 0.29, thus suggesting that AN molecules could be entrapped in these AGGs, explaining the thermal stability of the PMAPC1 + LiTFSI + AN electrolytes.

https://doi.org/10.1021/acsami.1c11058
ACS Appl. Mater. Interfaces 2021, 13, 44844−44859

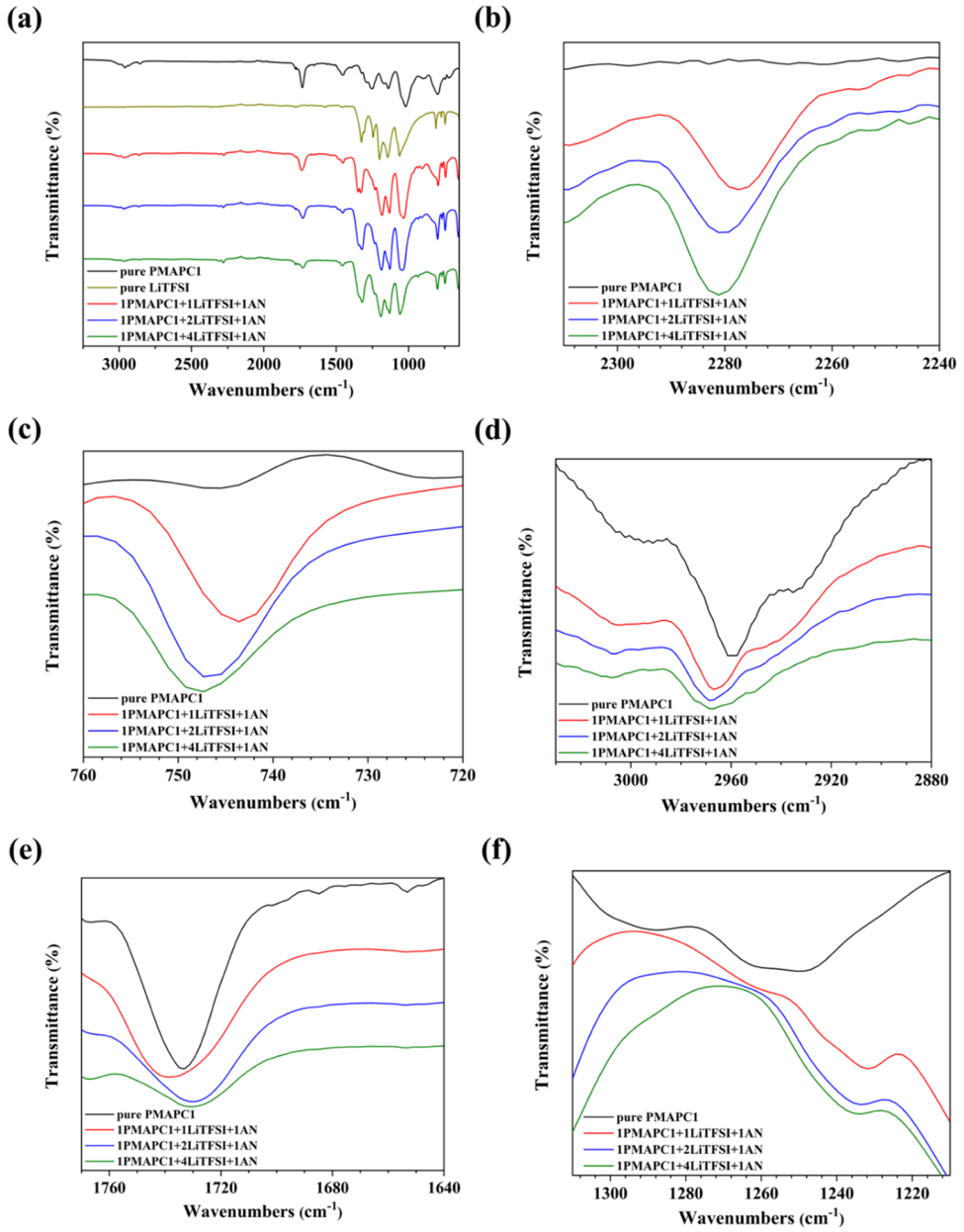

Figure 6. FTIR spectra of 1PMAPC1 + *x*LiTFSI + 1AN electrolyte (x = 1, 2, and 4) in (a) 650−3250 cm^{-1}, (b) 2240−2310 cm^{-1} (C≡N stretching mode of AN molecules), (c) 720−760 cm^{-1} (S−N stretching, C−S stretching, and CF_3 bending mode of $TFSI^-$), (d) 2880−3030 cm^{-1} (intramolecular interactions between C═O and C−H), (e) 1640−1770 cm^{-1} (C═O stretching mode of MAPC1 units), and (f) 1210−1310 cm^{-1} (P═O stretching mode of MAPC1 units).

Finally, FTIR spectra can be used to gain information about the interaction of PMAPC1 with Li^+ ions. In Figure 6d, the peak at approximately 2960 cm^{-1} observed for pure PMAPC1 can be attributed to dipolar interactions between C═O (−CO−O−CH_2−) and CH_2 groups (−CO−O−CH_2−) on two neighboring side chains of PMAPC1.[55] The intensity of this band decreases and shifts from 2960 to 2970 cm^{-1} when the LiTFSI concentration increases. This indicates that the intramolecular interactions between neighboring ester groups of PMAPC1 chains are canceled by the addition of LiTFSI, which confers higher mobility to PMAPC1 side chains.[45,55,56] In Figure 6e, the band at 1735 cm^{-1} can be assigned to the stretching vibration mode of the C═O on the side chains of PMAPC1. Since intramolecular interactions between C═O and CH_2 groups are suppressed upon addition of LiTFSI, the carbonyl groups can easily coordinate with Li^+ ions. The intensity of this peak decreases with increasing salt concentration, evidencing carbonyl−Li^+ interactions.[55] Finally, the P═O stretch in PMAPC1 corresponds to the broad band observed in the 1244−1262 cm^{-1} range, as shown in Figure 6f. This band immediately disappears when LiTFSI is added, in favor of a new band at 1232 cm^{-1}, indicating interactions between LiTFSI and P═O groups.[57,58] From the composition analysis of the coordination shells of Li^+ cations (Table S5), we find that these cations tend to interact with oxygen atoms of both C═O and P═O groups, the latter being predominant.

In view of these results, we propose the following hypothesis to explain ionic conduction in PMAPC1 + LiTFSI + AN electrolytes. The LiTFSI salt tends to form amorphous AGGs homogeneously entrapping AN molecules (according to Figure

https://doi.org/10.1021/acsami.1c11058
ACS Appl. Mater. Interfaces 2021, 13, 44844−44859

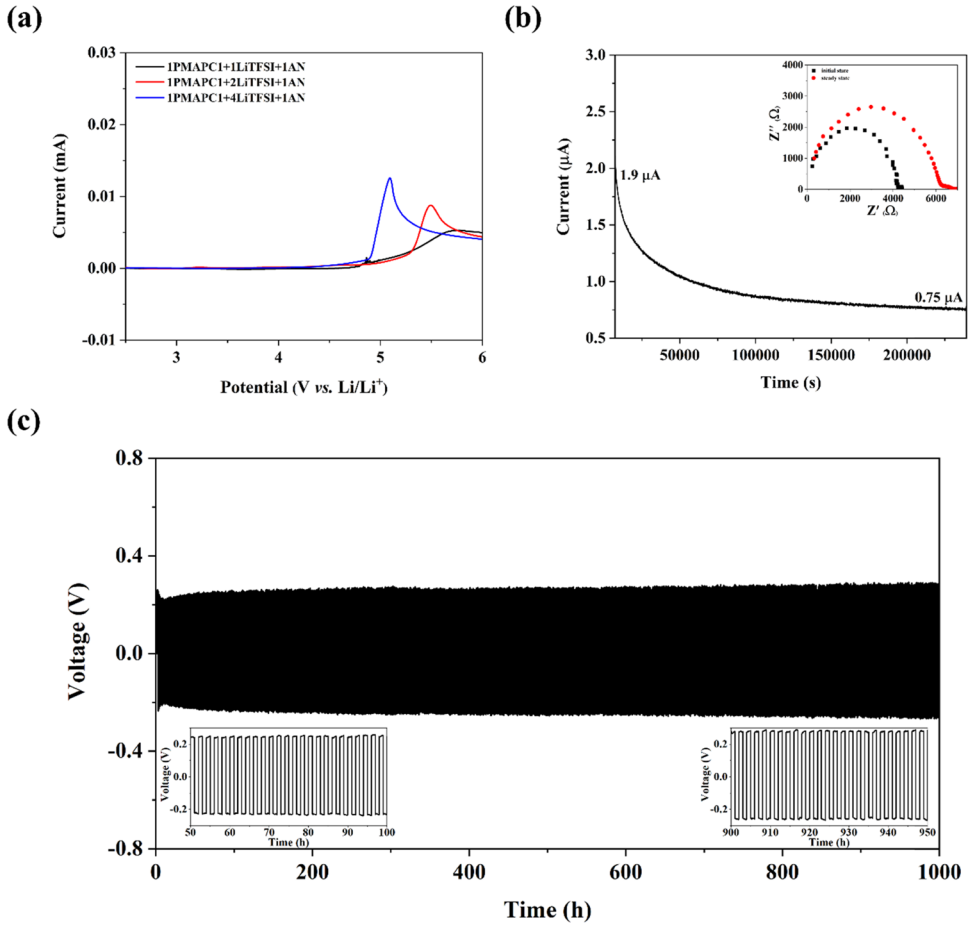

Figure 7. (a) Linear sweep voltammograms for blank 1PMAPC1 + 1LiTFSI + 1AN, 1PMAPC1 + 2LiTFSI + 1AN, and 1PMAPC1 + 4LiTFSI + 1AN samples at 60 °C with a scan rate of 1 mV s^{-1}. (b) Polarization curve, initial (in black) and steady state (in red) impedance diagram (inset) for the 1PMAPC1 + 2LiTFSI + 1AN electrolyte at 60 °C. (c) Galvanostatic cycling curves of the Li|1PMAPC1 + 2LiTFSI + 1AN|Li symmetric cell at a current density of 0.1 mA cm^{-2} at 60 °C.

4a, no crystallization is observed in AGGs until very high loading in LiTFSI is reached). AGGs can be easily exchanged intra- and intermolecularly between PMAPC1 chain segments contributing to the vehicular mechanism evidenced by MD simulations.

Free Li^+ and $TFSI^-$ ions are in equilibrium with those mixed AGGs, and Li^+ ions first interact with the P═O bond of the phosphonate groups of PMAPC1 and then with the C═O of the ester groups of PMAPC1 at the expense of dipolar interactions among PMAPC1 side chains. These free Li^+ ions likely contribute to the hopping mechanism observed in MD simulations and are ultimately responsible of the ionic conduction in the PMAPC1 + LiTFSI + AN electrolytes.

4.4. Electrochemical Properties of PMAPC1 + LiTFSI + AN Electrolytes. The electrochemical stability window of PMAPC1 + LiTFSI + AN electrolytes was evaluated by linear sweep voltammetry (LSV) in a stainless steel|SPE|Li cell with a potential range from 0 to 6.0 V. As shown in Figure 7a, the 1PMAPC1 + *x*LiTFSI + 1AN electrolyte displays an electrochemical stability window up to 4.7 V, no obvious oxidation peak or apparent anodic current being observed below 4.7 V. This broad electrochemical window makes our SPEs suitable for batteries with high-voltage cathodes.

The lithium-ion transference number (t_{Li}^+), defined as the ratio of the electric current derived from the cations to the total electric current,[59] is another crucial factor to characterize the electrolyte performance. Figure 7b shows the time-dependent response of a Li|1PMAPC1 + 2LiTFSI + 1AN|Li symmetric cell at 60 °C with an applied DC bias of 50 mV, while the EIS performed in the initial state and steady state are depicted in the inset. The t_{Li}^+ for the 1PMAPC1 + 2LiTFSI + 1AN electrolyte has been calculated to be 0.4 at 60 °C using Evans et al.'s equation.[60] This transference number exceeds that of linear PEO electrolytes, which is typically reported to be around 0.2.[40]

Galvanostatic cycling experiments have then been used to analyze the interface stability between our electrolytes and Li-metal electrodes. These experiments have been performed on Li symmetric cells repeatedly charged and discharged for 1 h with a constant current density of 0.1 mA cm^{-2} at 60 °C. Constant stable negative and positive voltage plateaus have been observed for the Li|1PMAPC1 + 2LiTFSI + 1AN|Li cell reflecting a stable interface formed on the Li metal during plating/stripping over time (Figure 7c). The Li|1PMAPC1 + 1LiTFSI + 1AN|Li cell shows a sudden increase in potentials after 150 h, and then stabilizes at 0.2 V after 300 h, which could be attributed to unstable interfacial reactions of AN with the Li metal (Figure S9a). The Li|1PMAPC1 + 4LiTFSI + 1AN|Li cell exhibits fluctuations after 200 h of cycling, which are ascribed to the decomposition of LiTFSI and continuous formation of the SEI layer resulting in an increase in impedance and polarization (Figure S9b). These results

https://doi.org/10.1021/acsami.1c11058
ACS Appl. Mater. Interfaces 2021, 13, 44844−44859

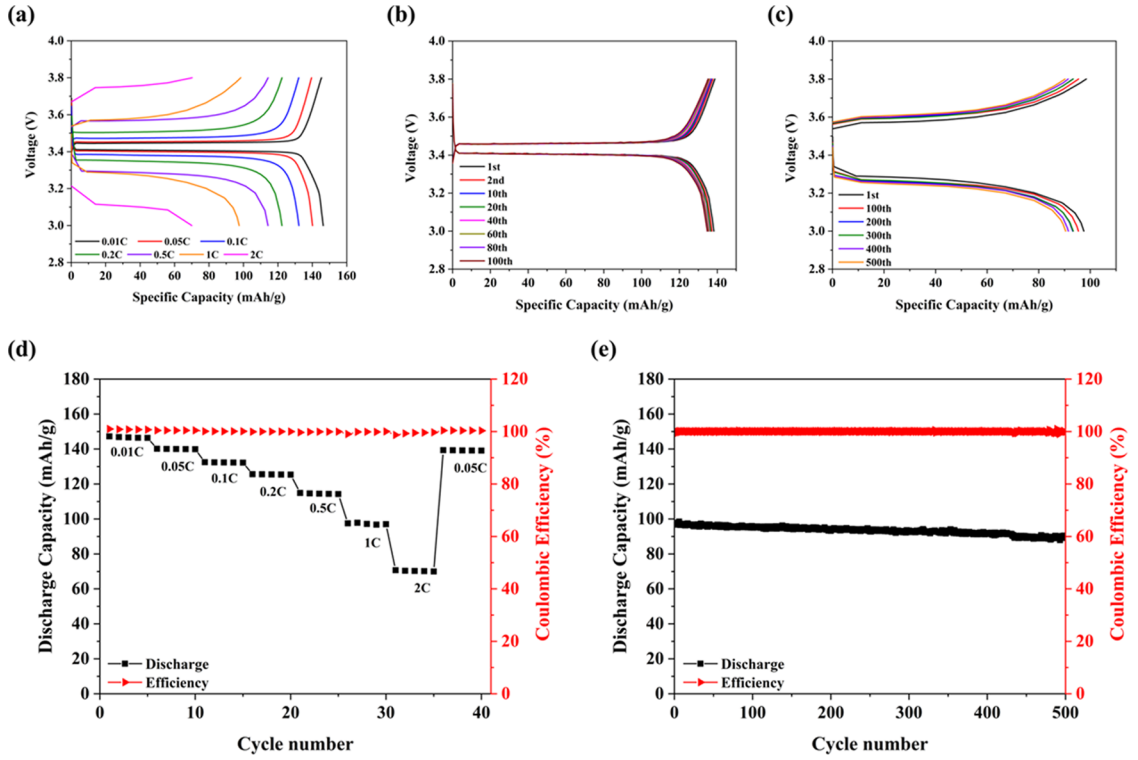

Figure 8. (a) Initial charge and discharge voltage profiles of a $LiFePO_4$|1PMAPC1 + 2LiTFSI + 1AN|Li cell under different rates at 60 °C. (b) Under 0.2 C at 60 °C for 100 cycles. (c) Under 1 C at 60 °C for 500 cycles. (d) Rate performance. (e) Cycling performance under 1 C at 60 °C.

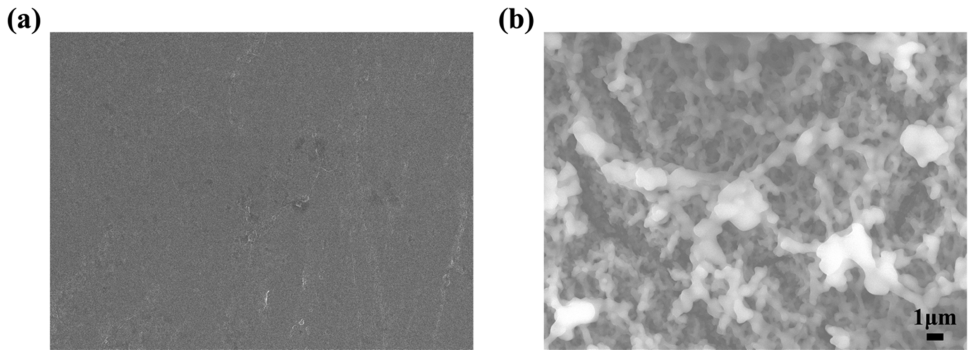

Figure 9. (a) SEM images of the lithium anode before and (b) after 100 cycles charge and discharge of the $LiFePO_4$|1PMAPC1 + 2LiTFSI + 1AN|Li cell at a 0.05 C rate.

further confirm that the 1PMAPC1 + 2LiTFSI + 1AN electrolyte is the best candidate to be tested in a battery prototype.

4.5. Testing PMAPC1 + LiTFSI + AN Electrolytes in a Battery Prototype. The 1PMAPC1 + 2LiTFSI + 1AN electrolyte was assembled with a $LiFePO_4$ cathode and a Li-metal anode to demonstrate its applicability in a solid-state LMB. Details about the assembly process leading to $LiFePO_4$|1PMAPC1 + 2LiTFSI + 1AN|Li cells are provided in Figure S10. Figure 8a shows the initial charge−discharge voltage curves of the $LiFePO_4$|1PMAPC1 + 2LiTFSI + 1AN|Li cell at various rates from 0.01 to 2 C in the 3.0−3.8 V voltage range at 60 °C. The cell exhibits discharge capacities of ≈147.2, 140.1, 132.5, 125.6, 114.8, 97.5, and 70.7 mAh g^{-1} at different rates of 0.01, 0.05, 0.1, 0.2, 0.5, 1, and 2 C, respectively. Figure 8b shows typical charge−discharge voltage profiles at 0.2 C with the two initials, the 10th, the 20th, the 40th, the 60th, the 80th, and the 100th cycles in a 3.0−3.8 V voltage range at 60 °C, demonstrating that the polarization effect is weak at low cycling rates. During the cycling, an initial specific capacity of 140.1 mAh g^{-1} and a capacity retention as high as 96.4% after 100 cycles are measured, demonstrating the interesting electrochemical performance of the $LiFePO_4$|1PMAPC1 + 2LiTFSI + 1AN|Li battery. In Figure 8c, stable potential curves are achieved at 1 C despite a large polarization effect, and the capacity retention reaches 91.4% after 500 cycles. The cycling performances at various current rates from 0.01 to 2 C at 60 °C are presented in Figure 8d. When the current is restored to 0.05 C after several cycles at higher rates, the discharge capacities are recovered to 139 mAh g^{-1}, reaching 99.3% of the initial discharge capacity at 0.05 C. Finally, Figure 8e shows the discharge capacity and Coulombic efficiency versus cycle number at 1 C. The initial discharge capacity of the cell is 97.5 mAh g^{-1} and its Coulombic efficiency is 99.8%. There is no significant decay of the discharge capacity after 500 cycles, and the reversible capacity is maintained at 89.1 mAh g^{-1} with a

https://doi.org/10.1021/acsami.1c11058
ACS Appl. Mater. Interfaces 2021, 13, 44844−44859

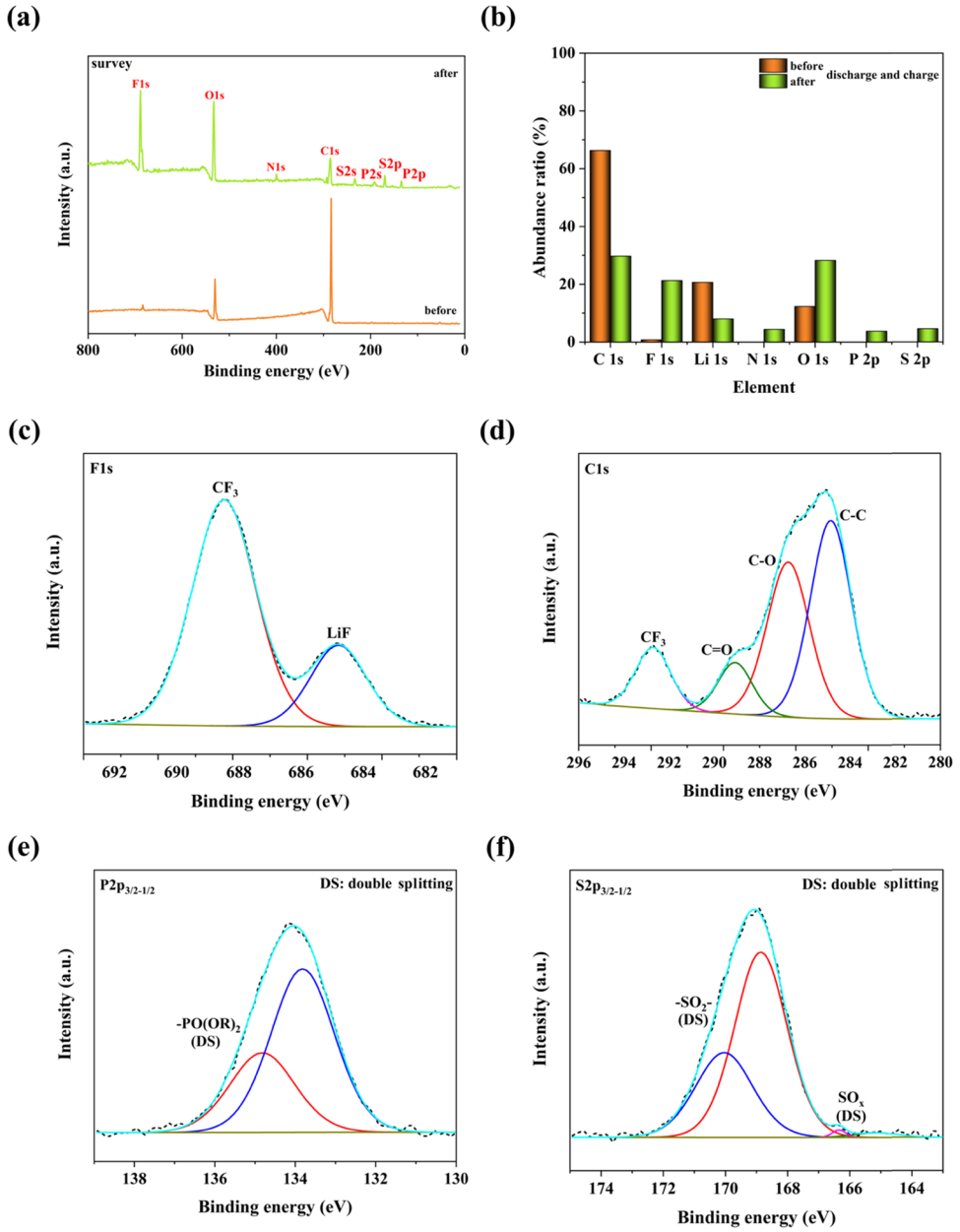

Figure 10. (a) Wide-scan XPS spectrum of the lithium-metal anode before and after 100 cycles of charge and discharge of the $LiFePO_4$|1PMAPC1 + 2LiTFSI + 1AN|Li cell at a 0.05 C rate. (b) Atomic ratios of C, O, F, S, P, and N on the surface of the lithium anode obtained from the XPS spectra. (c) F 1s. (d) C 1s. (e) P 2p. (f) S 2p spectra. Points and solid lines denote experimental spectra and fitting curves, respectively.

Coulombic efficiency of 99%, corresponding to a capacity retention of 91.4%. Figure S11a shows long cycling performances at various current rates from 0.01 to 1 C at 60 °C. Figure S11b−e shows the discharge capacity and Coulombic efficiency for 100 cycles at 0.05, 0.1, 0.2, and 0.5 C, respectively, and confirms the excellent results obtained for the $LiFePO_4$|1PMAPC1 + 2LiTFSI + 1AN|Li cell.

The excellent cycling stability of the $LiFePO_4$|1PMAPC1 + 2LiTFSI + 1AN|Li cell is mainly attributed to the formation of a stable interface between the electrolyte and the anode. This will be confirmed in the next section.

4.6. Postmortem Analysis of the Battery Prototype and the Study of the Electrolyte/Anode Interface. To understand the outstanding cycling stability of the $LiFePO_4$|1PMAPC1 + 2LiTFSI + 1AN|Li cell, a postmortem analysis of the disassembled cell after 100 cycles was conducted. In a first step, scanning electron microscopy (SEM) analysis of the disassembled Li-metal anode has been realized to visualize whether Li dendrites have formed. Figure 9 shows a uniform porous film formed by micrometer particles at the surface of the Li anode but no Li dendrites. This film originates from the decomposition of the 1PMAPC1 + 2LiTFSI + 1AN electrolyte in contact with the Li-metal, resulting in a stable solid-electrolyte interphase (SEI). Obviously, the SEI formed in our SPEs can effectively suppress the growth of lithium dendrites,[61] and its ionic conductivity[62] is sufficient to allow the excellent electrochemical performances measured in the previous section. It has been reported that fluorinated SEIs are particularly stable and can enhance the safety of Li-metal batteries by regulating Li deposition.[24,63] Moreover, LiTFSI is known to decompose during cycling to form a fluorinated SEI,[64] with a high LiF content.[65] This ultimately leads to

https://doi.org/10.1021/acsami.1c11058
ACS Appl. Mater. Interfaces 2021, 13, 44844−44859

dendrite-free, superior cycling performance and higher efficiency batteries.[66]

To assess the formation of a LiF-rich SEI in the $LiFePO_4$|1PMAPC1 + 2LiTFSI + 1AN|Li cell, X-ray photoelectron spectroscopy (XPS) was performed on the SEI formed on the Li-metal anode before and after 100 cycles of charge−discharge. The C 1s peak at 284.8 eV was used as a reference to calibrate the binding energy. All of the peaks were assigned based on previous reports.[30,67,68] Before the charge−discharge test (1PMAPC1 + 2LiTFSI + 1AN electrolyte touched with the lithium foil for 24 h, and removed), the major surface elements were C and O from the atmosphere, which reacted with lithium. A quite low amount of the F element should originate from the residual LiTFSI in the electrolyte. This indicates that the remaining electrolyte components on the surface of lithium are negligible. After 100 cycles of charge and discharge, the results indicate that a SEI film containing mainly C, F, and O and small amounts of P, S, and N is formed on the surface of the lithium metal (Figure 10a,b). The F 1s spectrum (Figure 10c) shows the presence of two components. The peak observed at low binding energy (685.0−685.2 eV) is typical of LiF.[69] The peak at higher binding energy can be assigned to a CF_3 peak. Both species should arise from the decomposition of $TFSI^-$ anions on the Li-metal anode. The analysis of the C 1s region (Figure 10d) reveals four peaks attributed to C−C, C−O, C═O, and CF_3. These species originate from the decomposition of PMAPC1, $TFSI^-$, and AN. The characteristic double-split peak in the P 2p spectrum (P $2p_{3/2}$ and P $2p_{1/2}$) arises from the decomposition of PMAPC1 (Figure 10e). In the S 2p spectrum (Figure 10f), the presence of spin−orbit split doublets (S $2p_{3/2}$ and S $2p_{1/2}$) is characteristic of $-SO_2-$ and SO_x, which are decomposition products of $TFSI^-$ anions. In the N 1s and O 1s spectra (Figure S12), the overlapping of peaks hinders the identification of the accurate chemical states. Since N atoms originate from AN and $TFSI^-$, the low intensity of the N signal is consistent with a limited degradation of AN molecules at the Li-metal anode. To sum up, the XPS measurements confirm the formation of a LiF-rich SEI that is highly beneficial to the electrochemical performances of our $LiFePO_4$|1PMAPC1 + 2LiTFSI + 1AN|Li cells. These results are also consistent with a limited degradation of AN in contact with the Li metal.

5. CONCLUSIONS

In this contribution, we have demonstrated that plasticized or quasi-solid polymer electrolytes based on a phosphorus-containing polymer PMAPC1, a high content of LiTFSI, and small amount of AN are characterized by flame-retardant properties, can form self-standing and flexible membranes, can suppress Li dendrite growth, and enhance the interface stability by forming a LiF-rich layer at the SPE/anode interface. Moreover, these SPEs exhibit acceptable ionic conductivity up to 1.6×10^{-3} S cm^{-1} at 100 °C, a wide electrochemical window above 4.7 V versus Li^+/Li, and a good lithium-ion transference number of 0.4 at 60 °C. For practical applications, $LiFePO_4$|PMAPC1 + LiTFSI + AN|Li batteries are assembled as LMB prototypes and exhibit a high discharge specific capacity around 100 mAh g^{-1} for 500 cycles at 60 °C, with a rate capability up to 1 C.

A combined theoretical and experimental approach has been used to get insight into the conduction mechanism operating in our SPEs. Both approaches point toward the formation of mixed aggregates of LiTFSI and AN that play a crucial role at several levels. First, they protect AN against reaction with lithium at the anode side. Second, these mixed aggregates plasticize the polymer matrix, simultaneously increasing the overall mobility and the ionic conductivity. These LiTFSI−AN aggregates are believed to be responsible not only for the mixed vehicular conduction mechanism as determined from the modeling data but can also act as reservoirs for free Li^+ and $TFSI^-$ ions that can be reversibly released from them and could be responsible for the hopping mechanism. Finally, the formation of these dynamic mixed amorphous aggregates can also explain why such high loading of LITFSI can be achieved in our SPEs without phase separation from the polymer matrix.

Although their ionic conductivity values are still modest, the plasticized or quasi-solid high salt-content polymer electrolytes investigated in this study display excellent mechanical, fire-retardant, and cycling properties, as well as an important electrochemical stability, making our approach worth further investigation with other fire-retardant polymers added with other types of plasticizers.

ASSOCIATED CONTENT

Supporting Information

The Supporting Information is available free of charge at https://pubs.acs.org/doi/10.1021/acsami.1c11058.

Synthesis, NMR, DSC, TGA, and EIS of PMAPC1; morphology, flammability tests, and rheology of electrolytes; assembly route in coin cells; rate and cycling performances of electrolytes; ex situ XPS spectra of electrolytes; and calculated diffusion coefficients, ionic transport regime, degree of uncorrelated ionic mobility, and radius and composition of the coordination shell for electrolytes (PDF)

Flammability test of electrolyte 1PEO + 2LiTFSI + 1AN (MP4)

Flammability test of electrolyte 1PMAPC1 + 2LiTFSI + 1AN (MP4)

AUTHOR INFORMATION

Corresponding Author

Jean-François Gohy − *Institute of Condensed Matter and Nanosciences, Université catholique de Louvain, B-1348 Louvain-la-Neuve, Belgium;* orcid.org/0000-0003-4169-1883; Email: jean-francois.gohy@uclouvain.be

Authors

Lu Bai − *Institute of Condensed Matter and Nanosciences, Université catholique de Louvain, B-1348 Louvain-la-Neuve, Belgium*

Sina Ghiassinejad − *Institute of Condensed Matter and Nanosciences, Université catholique de Louvain, B-1348 Louvain-la-Neuve, Belgium*

Jérémy Brassinne − *Institute of Condensed Matter and Nanosciences, Université catholique de Louvain, B-1348 Louvain-la-Neuve, Belgium*

Yang Fu − *Institute of Condensed Matter and Nanosciences, Université catholique de Louvain, B-1348 Louvain-la-Neuve, Belgium*

Jiande Wang − *Institute of Condensed Matter and Nanosciences, Université catholique de Louvain, B-1348 Louvain-la-Neuve, Belgium*

Hui Yang − *Institute of Condensed Matter and Nanosciences, Université catholique de Louvain, B-1348 Louvain-la-Neuve, Belgium*

Alexandru Vlad − *Institute of Condensed Matter and Nanosciences, Université catholique de Louvain, B-1348 Louvain-la-Neuve, Belgium;* orcid.org/0000-0002-0059-9119

Andrea Minoia − *Laboratory for Chemistry of Novel Materials, Materials Research Institute, University of Mons—UMONS, B-7000 Mons, Belgium*

Roberto Lazzaroni − *Laboratory for Chemistry of Novel Materials, Materials Research Institute, University of Mons—UMONS, B-7000 Mons, Belgium;* orcid.org/0000-0002-6334-4068

Complete contact information is available at: https://pubs.acs.org/10.1021/acsami.1c11058

Author Contributions

The manuscript was written through contributions of all authors. All authors have given approval to the final version of the manuscript.

Notes

The authors declare no competing financial interest.

■ ACKNOWLEDGMENTS

This research was supported by the China Scholarship Council. The molecular modeling activities are supported by FNRS through the EOS 2Dto3D project (grant 30489208) and the CÉCI program (grant 2.5020.11) and by the Walloon Region (ZENOBE Tier-1 facility, under grant 1117545). The authors are grateful to Dr. Claudio Quarti for his help and fruitful discussions.

■ REFERENCES

(1) Etacheri, V.; Marom, R.; Elazari, R.; Salitra, G.; Aurbach, D. Challenges in the Development of Advanced Li-Ion Batteries: A Review. *Energy Environ. Sci.* **2011**, *4*, 3243−3262.

(2) Armand, M.; Tarascon, J.-M. Building Better Batteries. *Nature* **2008**, *451*, 652−657.

(3) Miller, T. F.; Wang, Z. G.; Coates, G. W.; Balsara, N. P. Designing Polymer Electrolytes for Safe and High Capacity Rechargeable Lithium Batteries. *Acc. Chem. Res.* **2017**, *50*, 590−593.

(4) Zhang, Q.; Liu, K.; Ding, F.; Liu, X. Recent Advances in Solid Polymer Electrolytes for Lithium Batteries. *Nano Res.* **2017**, *10*, 4139−4174.

(5) Liu, X.; Li, X.; Li, H.; Wu, H. B. Recent Progress of Hybrid Solid-State Electrolytes for Lithium Batteries. *Chem. − Eur. J.* **2018**, *24*, 18293−18306.

(6) Mackanic, D. G.; Michaels, W.; Lee, M.; Feng, D.; Lopez, J.; Qin, J.; Cui, Y.; Bao, Z. Crosslinked Poly(Tetrahydrofuran) as a Loosely Coordinating Polymer Electrolyte. *Adv. Energy Mater.* **2018**, *8*, No. 1800703.

(7) Li, Y.; Sun, Z.; Liu, D.; Lu, S.; Li, F.; Gao, G.; Zhu, M.; Li, M.; Zhang, Y.; Bu, H.; Jia, Z.; Ding, S. Bacterial Cellulose Composite Solid Polymer Electrolyte With High Tensile Strength and Lithium Dendrite Inhibition for Long Life Battery. *Energy Environ. Mater.* **2020**, 434−443.

(8) Li, Y.; Sun, Z.; Shi, L.; Lu, S.; Sun, Z.; Shi, Y.; Wu, H.; Zhang, Y.; Ding, S. Poly(Ionic Liquid)-Polyethylene Oxide Semi-Interpenetrating Polymer Network Solid Electrolyte for Safe Lithium Metal Batteries. *Chem. Eng. J.* **2019**, *375*, No. 121925.

(9) Appetecchi, G. B.; Zane, D.; Scrosati, B. PEO-Based Electrolyte Membranes Based on LiBC4O8 Salt. *J. Electrochem. Soc.* **2004**, *151*, A1369.

(10) Croce, F.; Appetecchi, G. B.; Persi, L.; Scrosati, B. Nanocomposite Polymer Electrolytes for Lithium Batteries. *Nature* **1998**, *394*, 456−458.

(11) Tominaga, Y.; Yamazaki, K. Fast Li-Ion Conduction in Poly(Ethylene Carbonate)-Based Electrolytes and Composites Filled with TiO2 Nanoparticles. *Chem. Commun.* **2014**, *50*, 4448−4450.

(12) Chintapalli, M.; Timachova, K.; Olson, K. R.; Banaszak, M.; Thelen, J. L.; Mecham, S. J.; Desimone, J. M.; Balsara, N. P. Incipient Microphase Separation in Short Chain Perfluoropolyether-: Block-Poly(Ethylene Oxide) Copolymers. *Soft Matter* **2017**, *13*, 4047−4056.

(13) Ionescu-Vasii, L. L.; Garcia, B.; Armand, M. Conductivities of Electrolytes Based on PEI-b-PEO-b-PEI Triblock Copolymers with Lithium and Copper TFSI Salts. *Solid State Ionics* **2006**, *177*, 885−892.

(14) Cui, Y.; Liang, X.; Chai, J.; Cui, Z.; Wang, Q.; He, W.; Liu, X.; Liu, Z.; Cui, G.; Feng, J. High Performance Solid Polymer Electrolytes for Rechargeable Batteries: A Self-Catalyzed Strategy toward Facile Synthesis. *Adv. Sci.* **2017**, *4*, No. 1700174.

(15) Xu, T.; Zhang, L.; Cheng, Z.; Zhu, X. Recent Advances in "Living"/Controlled Radical Polymerization of Phosphorus-Containing Monomers and Their Potential Applications. *Sci. China Chem.* **2015**, *58*, 1633−1640.

(16) Zheng, J.; Zhao, Y.; Feng, X.; Chen, W.; Zhao, Y. Novel Safer Phosphonate-Based Gel Polymer Electrolytes for Sodium-Ion Batteries with Excellent Cycling Performance. *J. Mater. Chem. A* **2018**, *6*, 6559−6564.

(17) Zheng, Q.; Yamada, Y.; Shang, R.; Ko, S.; Lee, Y. Y.; Kim, K.; Nakamura, E.; Yamada, A. A Cyclic Phosphate-Based Battery Electrolyte for High Voltage and Safe Operation. *Nat. Energy* **2020**, *5*, 291−298.

(18) Yao, X. L.; Xie, S.; Chen, C. H.; Wang, Q. S.; Sun, J. H.; Li, Y. L.; Lu, S. X. Comparative Study of Trimethyl Phosphite and Trimethyl Phosphate as Electrolyte Additives in Lithium Ion Batteries. *J. Power Sources* **2005**, *144*, 170−175.

(19) Xu, K.; Zhang, S.; Allen, J. L.; Jow, T. R. Nonflammable Electrolytes for Li-Ion Batteries Based on a Fluorinated Phosphate. *J. Electrochem. Soc.* **2002**, *149*, A1079−A1082.

(20) Kalhoff, J.; Bresser, D.; Bolloli, M.; Alloin, F.; Sanchez, J. Y.; Passerini, S. Enabling LiTFSI-Based Electrolytes for Safer Lithium-Ion Batteries by Using Linear Fluorinated Carbonates as (Co)Solvent. *ChemSusChem* **2014**, *7*, 2939−2946.

(21) Abouimrane, A.; Ding, J.; Davidson, I. J. Liquid Electrolyte Based on Lithium Bis-Fluorosulfonyl Imide Salt: Aluminum Corrosion Studies and Lithium Ion Battery Investigations. *J. Power Sources* **2009**, *189*, 693−696.

(22) Yamada, Y.; Wang, J.; Ko, S.; Watanabe, E.; Yamada, A. Advances and Issues in Developing Salt-Concentrated Battery Electrolytes. *Nat. Energy* **2019**, *4*, 269−280.

(23) Yamada, Y.; Chiang, C. H.; Sodeyama, K.; Wang, J.; Tateyama, Y.; Yamada, A. Corrosion Prevention Mechanism of Aluminum Metal in Superconcentrated Electrolytes. *ChemElectroChem* **2015**, *2*, 1687−1694.

(24) Li, T.; Zhang, X. Q.; Shi, P.; Zhang, Q. Fluorinated Solid-Electrolyte Interphase in High-Voltage Lithium Metal Batteries. *Joule* **2019**, *3*, 2647−2661.

(25) Mizuno, F.; Nakanishi, S.; Shirasawa, A.; Takechi, K.; Shiga, T.; Nishikoori, H.; Hideki, I. B. A. Design of Non-Aqueous Liquid Electrolytes for Rechargeable Li-O2 Batteries. *Electrochemistry* **2011**, *79*, 876−881.

(26) Peng, Z.; Freunberger, S. A.; Hardwick, L. J.; Chen, Y.; Giordani, V.; Bardé, F.; Novák, P.; Graham, D.; Tarascon, J. M.; Bruce, P. G. Oxygen Reactions in a Non-Aqueous Li+ Electrolyte. *Angew. Chem., Int. Ed.* **2011**, *50*, 6351−6355.

(27) Furukawa, K.; Kikuchi, K.; Yamada, A.; Sodeyama, K.; Yamada, Y.; Tateyama, Y.; Yaegashi, M. Unusual Stability of Acetonitrile-Based Superconcentrated Electrolytes for Fast-Charging Lithium-Ion Batteries. *J. Am. Chem. Soc.* **2014**, *136*, 5039−5046.

(28) Younesi, R.; Veith, G. M.; Johansson, P.; Edström, K.; Vegge, T. Lithium Salts for Advanced Lithium Batteries: Li-Metal, Li-O2, and Li-S. *Energy Environ. Sci.* **2015**, *8*, 1905−1922.
(29) Pohl, B.; Wiemhöfer, H. D. Highly Thermal and Electrochemical Stable Dinitrile Disiloxane as Co-Solvent for Use in Lithium-Ion Batteries. *J. Electrochem. Soc.* **2015**, *162*, A460−A464.
(30) Yamada, Y.; Furukawa, K.; Sodeyama, K.; Kikuchi, K.; Yaegashi, M.; Tateyama, Y.; Yamada, A. Unusual Stability of Acetonitrile-Based Superconcentrated Electrolytes for Fast-Charging Lithium-Ion Batteries. *J. Am. Chem. Soc.* **2014**, *136*, 5039−5046.
(31) Abraham, M. J.; Murtola, T.; Schulz, R.; Páll, S.; Smith, J. C.; Hess, B.; Lindah, E. Gromacs: High Performance Molecular Simulations through Multi-Level Parallelism from Laptops to Supercomputers. *SoftwareX* **2015**, *1−2*, 19−25.
(32) Jorgensen, W. L.; Maxwell, D. S.; Tirado-Rives, J. Development and Testing of the OPLS All-Atom Force Field on Conformational Energetics and Properties of Organic Liquids. *J. Am. Chem. Soc.* **1996**, *118*, 11225−11236.
(33) Salanne, M. Simulations of Room Temperature Ionic Liquids: From Polarizable to Coarse-Grained Force Fields. *Phys. Chem. Chem. Phys.* **2015**, *17*, 14270−14279.
(34) Chaudhari, M. I.; Nair, J. R.; Pratt, L. R.; Soto, F. A.; Balbuena, P. B.; Rempe, S. B. Scaling Atomic Partial Charges of Carbonate Solvents for Lithium Ion Solvation and Diffusion. *J. Chem. Theory Comput.* **2016**, *12*, 5709−5718.
(35) Bis(trifluoromethane)sulfonimide Lithium Salt—CAS-Number 90076-65-6—Order from Chemodex. https://www.chemodex.com/products/bistrifluoromethanesulfonimide-lithium-salt/ (accessed Jan 14, 2021).
(36) Borodin, O. Polarizable Force Field Development and Molecular Dynamics Simulations of Ionic Liquids. *J. Phys. Chem. B* **2009**, *113*, 11463−11478.
(37) El Asri, Z.; Chougrani, K.; Negrell-Guirao, C.; David, G.; Boutevin, B.; Loubat, C. An Efficient Process for Synthesizing and Hydrolyzing a Phosphonated Methacrylate: Investigation of the Adhesive and Anticorrosive Properties. *J. Polym. Sci., Part A: Polym. Chem.* **2008**, *46*, 4794−4803.
(38) Canniccioni, B.; Monge, S.; David, G.; Robin, J. J. RAFT Polymerization of Dimethyl(Methacryloyloxy)Methyl Phosphonate and Its Phosphonic Acid Derivative: A New Opportunity for Phosphorus-Based Materials. *Polym. Chem.* **2013**, *4*, 3676−3685.
(39) Agrawal, R. C.; Pandey, G. P. Solid Polymer Electrolytes: Materials Designing and All-Solid-State Battery Applications: An Overview. *J. Phys. D: Appl. Phys.* **2008**, *41*, No. 223001.
(40) Long, L.; Wang, S.; Xiao, M.; Meng, Y. Polymer Electrolytes for Lithium Polymer Batteries. *J. Mater. Chem. A* **2016**, *4*, 10038−10039.
(41) Xu, W.; Wang, J.; Ding, F.; Chen, X.; Nasybulin, E.; Zhang, Y.; Zhang, J. G. Lithium Metal Anodes for Rechargeable Batteries. *Energy Environ. Sci.* **2014**, *7*, 513−537.
(42) Ferry, J. D. *Viscoelastic Properties of Polymers*, 3rd ed.; John Wiley& Sons: New York, 1980.
(43) Akkaoui, K.; Yang, M.; Digby, Z. A.; Schlenoff, J. B. Ultraviscosity in Entangled Polyelectrolyte Complexes and Coacervates. *Macromolecules* **2020**, *53*, 4234−4246.
(44) Hird, B.; Eisenberg, A. Sizes and Stabilities of Multiplets and Clusters in Carboxylated and Sulfonated Styrene Ionomers. *Macromolecules* **1992**, *25*, 6466−6474.
(45) Tao, C.; Gao, M. H.; Yin, B. H.; Li, B.; Huang, Y. P.; Xu, G.; Bao, J. J. A Promising TPU/PEO Blend Polymer Electrolyte for All-Solid-State Lithium Ion Batteries. *Electrochim. Acta* **2017**, *257*, 31−39.
(46) Pehlivan, I. B.; Marsal, R.; Niklasson, G. A.; Granqvist, C. G.; Georén, P. PEI-LiTFSI Electrolytes for Electrochromic Devices: Characterization by Differential Scanning Calorimetry and Viscosity Measurements. *Sol. Energy Mater. Sol. Cells* **2010**, *94*, 2399−2404.
(47) Mindemark, J.; Imholt, L.; Montero, J.; Brandell, D. Allyl Ethers as Combined Plasticizing and Crosslinkable Side Groups in Polycarbonate-Based Polymer Electrolytes for Solid-State Li Batteries. *J. Polym. Sci., Part A: Polym. Chem.* **2016**, *54*, 2128−2135.
(48) Loo, W. S.; Mongcopa, K. I.; Gribble, D. A.; Faraone, A. A.; Balsara, N. P. Investigating the Effect of Added Salt on the Chain Dimensions of Poly(Ethylene Oxide) through Small-Angle Neutron Scattering. *Macromolecules* **2019**, *52*, 8724−8732.
(49) Mongcopa, K. I. S.; Tyagi, M.; Mailoa, J. P.; Samsonidze, G.; Kozinsky, B.; Mullin, S. A.; Gribble, D. A.; Watanabe, H.; Balsara, N. P. Relationship between Segmental Dynamics Measured by Quasi-Elastic Neutron Scattering and Conductivity in Polymer Electrolytes. *ACS Macro Lett.* **2018**, *7*, 504−508.
(50) Rajendran, S.; Sivakumar, M.; Subadevi, R. Effect of Salt Concentration in Poly(Vinyl Alcohol)-Based Solid Polymer Electrolytes. *J. Power Sources* **2003**, *124*, 225−230.
(51) Kolosnitsyn, V. S.; Dukhanin, G. P.; Dumler, S. A.; Novakov, I. A. Lithium-Conducting Polymer Electrolytes for Chemical Power Sources. *Russ. J. Appl. Chem.* **2005**, *78*, 1−18.
(52) Bedrov, D.; Piquemal, J. P.; Borodin, O.; MacKerell, A. D.; Roux, B.; Schröder, C. Molecular Dynamics Simulations of Ionic Liquids and Electrolytes Using Polarizable Force Fields. *Chem. Rev.* **2019**, *119*, 7940−7995.
(53) Brouillette, D.; Irish, D. E.; Taylor, N. J.; Perron, G.; Odziemkowski, M.; Desnoyers, J. E. Stable Solvates in Solution of Lithium Bis(Trifluoromethylsulfone)Imide in Glymes and Other Aprotic Solvents: Phase Diagrams, Crystallography and Raman Spectroscopy. *Phys. Chem. Chem. Phys.* **2002**, *4*, 6063−6071.
(54) Seo, D. M.; Borodin, O.; Han, S.-D.; Boyle, P. D.; Henderson, W. A. Electrolyte Solvation and Ionic Association II. Acetonitrile-Lithium Salt Mixtures: Highly Dissociated Salts. *J. Electrochem. Soc.* **2012**, *159*, A1489−A1500.
(55) Motomatsu, J.; Kodama, H.; Furukawa, T.; Tominaga, Y. Dielectric Relaxation Behavior of a Poly(Ethylene Carbonate)-Lithium Bis-(Trifluoromethanesulfonyl) Imide Electrolyte. *Macromol. Chem. Phys.* **2015**, *216*, 1660−1665.
(56) Tominaga, Y.; Yamazaki, K.; Nanthana, V. Effect of Anions on Lithium Ion Conduction in Poly(Ethylene Carbonate)-Based Polymer Electrolytes. *J. Electrochem. Soc.* **2015**, *162*, A3133−A3136.
(57) Cataldo, F. Surface Interaction and Desorption of Trimethyl Phosphate from Ozonized Activated Carbon Fabric. *Fullerenes, Nanotubes, Carbon Nanostruct.* **2018**, *26*, 379−388.
(58) Mastrantonio, G.; Védova, C. O. D. Spectroscopic and Conformational Comparative Study of Trimethyl Chalcogenphosphates. *J. Mol. Struct.* **2001**, *561*, 161−174.
(59) Ye, L.; Feng, Z. Polymer Electrolytes as Solid Solvents and Their Applications. *Polym. Electrolytes* **2010**, 550−582.
(60) Evans, J.; Vincent, C. A.; Bruce, P. G. Electrochemical Measurement of Transference Numbers in Polymer Electrolytes. *Polymer* **1987**, *28*, 2324−2328.
(61) Li, W.; Yao, H.; Yan, K.; Zheng, G.; Liang, Z.; Chiang, Y. M.; Cui, Y. The Synergetic Effect of Lithium Polysulfide and Lithium Nitrate to Prevent Lithium Dendrite Growth. *Nat. Commun.* **2015**, *6*, No. 7436.
(62) Piao, N.; Ji, X.; Xu, H.; Fan, X.; Chen, L.; Liu, S.; Garaga, M. N.; Greenbaum, S. G.; Wang, L.; Wang, C.; He, X. Countersolvent Electrolytes for Lithium-Metal Batteries. *Adv. Energy Mater.* **2020**, *10*, No. 1903568.
(63) Fan, X.; Ji, X.; Han, F.; Yue, J.; Chen, J.; Chen, L.; Deng, T.; Jiang, J.; Wang, C. Fluorinated Solid Electrolyte Interphase Enables Highly Reversible Solid-State Li Metal Battery. *Sci. Adv.* **2018**, *4*, No. eaau9245.
(64) Shi, P.; Zhang, L.; Xiang, H.; Liang, X.; Sun, Y.; Xu, W. Lithium Difluorophosphate as a Dendrite-Suppressing Additive for Lithium Metal Batteries. *ACS Appl. Mater. Interfaces* **2018**, *10*, 22201−22209.
(65) Lang, J.; Long, Y.; Qu, J.; Luo, X.; Wei, H.; Huang, K.; Zhang, H.; Qi, L.; Zhang, Q.; Li, Z.; Wu, H. One-Pot Solution Coating of High Quality LiF Layer to Stabilize Li Metal Anode. *Energy Storage Mater.* **2019**, *16*, 85−90.
(66) Kim, H.; Lee, J. T.; Yushin, G. High Temperature Stabilization of Lithium-Sulfur Cells with Carbon Nanotube Current Collector. *J. Power Sources* **2013**, *226*, 256−265.

(67) Leroy, S.; Blanchard, F.; Dedryvère, R.; Martinez, H.; Carré, B.; Lemordant, D.; Gonbeau, D. Surface Film Formation on a Graphite Electrode in Li-Ion Batteries: AFM and XPS Study. *Surf. Interface Anal.* **2005**, *37*, 773−781.
(68) Leroy, S.; Martinez, H.; Dedryvère, R.; Lemordant, D.; Gonbeau, D. Influence of the Lithium Salt Nature over the Surface Film Formation on a Graphite Electrode in Li-Ion Batteries: An XPS Study. *Appl. Surf. Sci.* **2007**, *253*, 4895−4905.
(69) Grissa, R.; Fernandez, V.; Fairley, N.; Hamon, J.; Stephant, N.; Rolland, J.; Bouchet, R.; Lecuyer, M.; Deschamps, M.; Guyomard, D.; Moreau, P. XPS and SEM-EDX Study of Electrolyte Nature Effect on Li Electrode in Lithium Metal Batteries. *ACS Appl. Energy Mater.* **2018**, *1*, 5694−5702.

https://doi.org/10.1021/acsami.1c11058
ACS Appl. Mater. Interfaces 2021, 13, 44844−44859